Looking into the structure of bijel-templated membranes

Cos Hesseling

UTRECHT UNIVERSITY

MASTER THESIS

Looking into the structure of bijel templated membranes

Cos HESSELING

Supervisors:
dr. Martin F. HAASE
Mariska de RUITER
Henrik SIEGEL

December 9, 2022

Abstract

Desalination of seawater is an increasingly necessary process as climate change and population growth are making fresh water more scarce. The high energy requirements of this process can be reduced using membrane technology. Solvent transfer induced phase separation (STrIPS) is a recent approach to make porous membranes. In this method spindodal decomposition of oil and water is induced by removal of a solvent. This results in two intertwined and continuous phases with high interfacial area, of which the structure mechanically jammed by self-assembly of nanoparticles on the interface. We use the monomeric (1,4-butanediol diacrylate (BDA)), which is polymerized to obtain a solid membrane.

The aim of this work is to investigate if we can continuously produce thin-film bijel-templated membranes with a controllable structure, and if we can understand the mechanism of the formation of their structure. We look have looked into the production process by first building a roll-to-roll processing machine that is able to continuously produce the membranes, and by investigating the wetting behaviour of precursor mixtures on the substrate. The membrane structure and its formation mechanism were investigated by varying parameters such as nanoparticle concentration and surface chemistry, and by arresting phase separation at different time steps. The resulting structures were visualized using Laser Scanning Confocal Microscopy (LSCM) and Scanning Electron Microscopy (SEM).

With this research, we have improved the roll-to-roll fabrication method and have found how precursor composition which wet the substrate better result in membranes with a more homogeneous morphology. We learned how we can introduce vertical channels into the membrane structure by increasing the particle hydrophobicity, and how the pore size gradient can be decreased by increasing nanoparticle concentration. Furthermore, by tracking the structural evolution, we have found how phase separation progresses through the membranes, and how the surface pores are a deciding factor in formation process.

Contents

Introduction

Clean drinking water is essential to life on earth, but many people in developing countries still lack reliable access[1]. Furthermore, this problem is exacerbated by pollution of existing water sources, growing population, and increasing frequency of droughts due to climate change[2]. A promising solution for creating clean drinking water is in membrane separation processes as these are relatively facile and require lower energy than thermal separation processes[3, 4]. Membranes are generally produced by precipitation of polymers via the non-solvent-induced phase separation (NIPS) method[5]. The inclusion of nanoparticles into such membranes can provide a range of additional properties to a membrane. The resulting nanocomposite membranes can have a range of properties such as antifouling, antibacterial, absorptive, and catalytic, depending on the nanoparticles that are included[6, 7].

A promising technique for creating nanocomposite membranes is Solvent Transfer Induced Phase Separation (STrIPS)[8, 9]. This method arrest the spinodal decomposition of two immiscible liquids by jamming the interface with nanoparticles to create a bicontinuous interfacially jammed emulsion gel (bijel). This soft material has the benefit of having two highly intertwined liquid networks that allow separated flows through them. This has the potential of separating feed and filtrate by a particle layer that can act as membrane. This has already been applied for extraction purposes[10], but not yet for direct filtration. The bijel structure has been used as a template for a separation membrane by polymerizing one phase, and achieving size exclusion by tuning the surface pore size[11].

In most previous work, bijels have been made as fibre morphologies, but planar bijels offer the opportunity of easier upscalability. Planar bijel films have been produced in batch processes using various methods such as STrIPS[8], and Vapour-Induced Phase Separation (VIPS)[12]. Batch processes are, however, unsuitable for upscaling, and continuous methods such as roll-to-roll fabrication are preferred. Recently, a roll-to-roll coating machine has been designed in our group, and this work will continue to build on, and expand the knowledge obtained in this process[13].

The aim of this work is to make steps towards the optimization of the production of planar bijel templated membranes, as well as to understand its structural formation and how to control this. To this end, a prototype roll-to-roll bijel coating machine is built and tested with precursor solutions of which the oil/water ratio, the nanoparticle concentration, and the nanoparticle surface chemistry is varied. Confocal and scanning electron microscopy are used as tools to assess the 3D structure of the resulting membranes and contact angle analysis is performed to visualize the precursor-substrate interaction which is critical in the film deposition process. This has led to an understanding of how to control the structure of the membranes, as well as how these structures are generated during the STrIPS process.

Theory

2.1 Bijels

A bicontinuous interfacially jammed emulsion gel, or bijel, is a soft material that consists of two highly interpenetrating bicontinuous liquid domains that are stabilized by self-assembly of nanoparticles on the interface. The existence of a bijel was first hypothesized by Stratford et al. in 2005, using computer simulations to show that thermal quenching of a colloidal suspension in a binary solvent could result in a bicontinuous particle stabilized gel[14]. Two years later, Herzig et al. were the first to go from theory to practice as they synthesized stable bijels[15]. These groups initially saw the potential of bijels as microreactors, as they can facilitate the in- and outflow of reactants through two different phases, and could provide catalytic activity through incorporation of catalytic nanoparticles. Since then, bijels have shown potential in a wide rang of applications, such as in liquid-liquid extraction[10], as electrodes[16, 17], and even in food foams[18, 19]. The following sections will build up to an understanding of bijels by discussing the mechanisms behind their formation, stabilization, and fabrication.

2.1.1 Emulsions

An emulsion is a dispersion of two immiscible liquids, where droplets of one phase are dispersed in the other. An emulsion can consist of oil droplets in water (O/W), water droplets in oil (W/O), or oil droplets in oil (O/O), although a polar and a non-polar oil are required for the latter[20].

The simplest way of making an emulsion is to shake a vial containing oil and water, this will turn it turbid as droplets of one phase within the other interfere with light. If this is left to rest for a moment, the mixture will return to the separate oil and water phases by itself. This happens because of the energy penalty related to an interface and the tendency of a system to minimize its free energy (Figure 2.1).
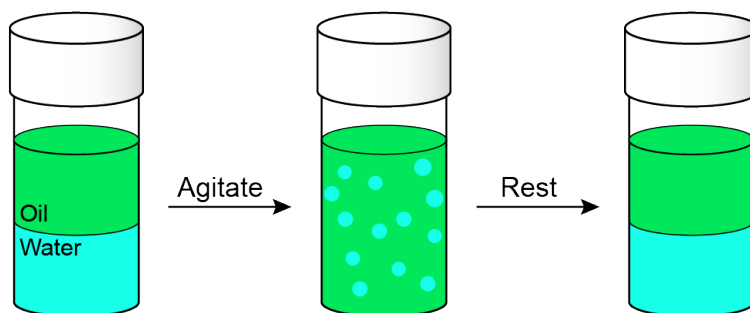

Figure 2.1: Mixing of oil (green) and water (cyan) leading to a water in oil emulsion, which returns to two separate phases after rest.

The energy penalty originates from the difference in environment of a molecule on an interface or in bulk. This originates from the partial positive or negative charges in polar

molecules attracting each other and forming hydrogen bonds. The most hydrogen bonds can be formed when a molecule is surrounded by similar polar molecules. At interfaces, the number of neighbouring polar molecules is lower, which results in the energy penalty.

The emulsion in Figure 2.1 is not stable because of surface tension, so to make a stable emulsion, the surface tension should be reduced. This is done by adding an emulsifier to the oil or water phase. An emulsifier must be a surface-active molecule that lowers the interfacial tension. Often, amphiphilic molecules are used as surfactants, as these molecules have a polar hydrophilic head group and a hydrophobic tail, and therefore stabilize a polar and non-polar liquid interface (Figure 2.2).
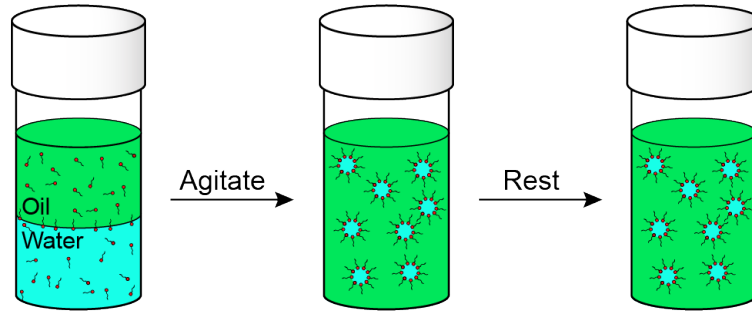

Figure 2.2: Mixing of oil (green) and water (cyan) with amphiphilic surfactant leads to stable emulsions.

2.1.2 Nanoparticle stabilized emulsions

In the beginning of the 20th century, Pickering[21] found that emulsions can also be stabilized using solid particles (Figure 2.3). Particles stabilize emulsions by decreasing the interfacial area between the two phases, and can be irreversibly attached to the interface[22]. The determining parameter for the strength of adsorption to the interface is the contact angle shown in Equation 2.1.
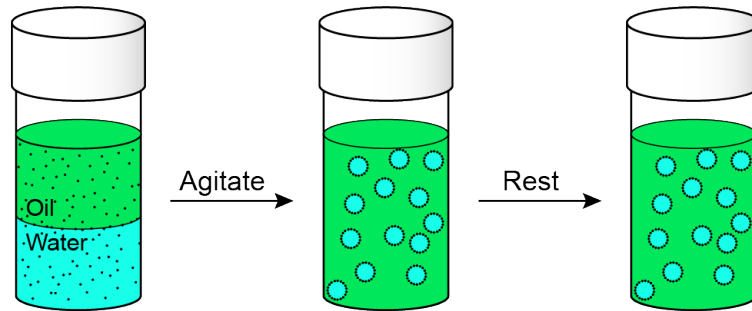
Figure 2.3: Mixing of oil (green) and water (cyan) with particles leads to stable Pickering emulsions.

$$\cos\theta = \frac{\gamma_{po} - \gamma_{pw}}{\gamma_{ow}} \qquad (2.1)$$

The contact angle is a balance between the particle-oil (γ_{po}), and particle-water (γ_{pw}) interfacial tensions, and the magnitude is determined by the oil-water interfacial tension (γ_{OW}). This means that if γ_{po} and γ_{pw} are close in value, or if the γ_{ow} is significantly greater than the two, the contact angle will be close to 90°, and the particle will be neutrally wetting. A neutrally wetting particle is ideal for stabilizing emulsions for two reasons. First, because attachment energy is increased, this will be shown in the next section. Second, because a contact angle of <90° preferentially stabilizes O/W emulsions, while a contact angle >90°

stabilizes W/O emulsions, a contact angle of 90° can stabilize both, and interfaces with inverting curvature (Figure 2.4).
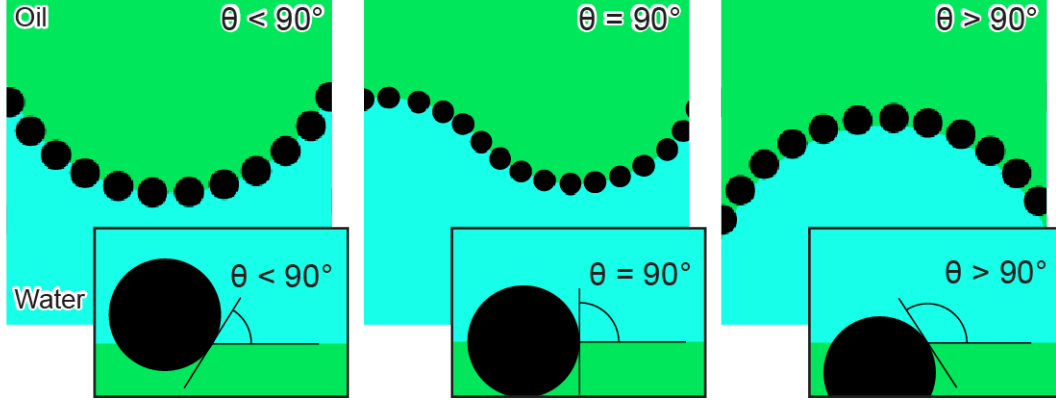

Figure 2.4: Schematic of particles stabilizing an o/w emulsion when the contact angle is below 90°, a w/o emulsion when the contact angle is above 90°, and a curved interface when the contact angle is 90°.

2.1.2.1 Nanoparticle attachment energy

The nanoparticle attachment energy is the change in surface free energy between a particle in one of two bulk phases and a particle at the oil-water interface[23]. We can calculate this by subtracting the interfacial Gibbs free energy of a particle in the bulk from the energy of a particle at the interface. We will for now treat the derivation as if the particle attaches to the interface while coming from the oil phase.
The interfacial Gibbs free energies at the interface and in bulk are given by equations 2.2 and 2.3, where G is the surface free energy, γ is the interfacial tension, and A the interfacial area. Superscripts ^{bo} and ^{i} denote the state of the particle being in the bulk and at the interface respectively, and the subscripts indicate oil-water (ow), particle-oil (po), particle-water (pw), or particle (p).

$$G^{bo} = A^b_{ow}\gamma_{ow} + A_p\gamma_{po} \tag{2.2}$$

$$G^i = A^i_{ow}\gamma_{ow} + A_{po}\gamma_{po} + A_{pw}\gamma_{pw} \tag{2.3}$$

If we then subtract equation 2.3 from equation 2.2 while using equation 2.1, and realizing that $A_{po} + A_{pw} = A_p$ we get an expression for the attachment energy from oil to the interface ΔG.

$$\Delta G_o = A^i_{ow}\gamma_{ow} + A_{po}\gamma_{po} + A_{pw}\gamma_{pw} - A^b_{ow}\gamma_{ow} - A_p\gamma_{po} \tag{2.4}$$

$$\Delta G_o = -\gamma_{ow}(A_c - A_{pw}\cos\theta) \tag{2.5}$$

Where $A_c = A^b_{ow} - A^i_{ow}$, which is the area that the particle decreases the oil-water interface with by adsorbing to the interface. In the case of spherical particles, we know that $A_c = \pi(r\sin\Theta)^2$ and that $A_{pw} = 2\pi r^2(1 + \cos\theta)$. Which allows us to rewrite equation 2.5 into:

$$\Delta G_o = -\pi r^2\gamma_{ow}(1 - \cos\theta)^2 \tag{2.6}$$

A similar derivation for a particle going from water to the interface leads to:

$$\Delta G_w = -\pi r^2\gamma_{ow}(1 + \cos\theta)^2 \tag{2.7}$$

By realizing that a for a particle with a contact between 0° and 90° $\Delta G = \Delta G_w$, and that for a particle with a contact angle between 90° and 180° $\Delta G = \Delta G_o$, we can combine

equations 2.6 and 2.7 into a final expression for the interfacial Gibbs free energy.

$$\Delta G = -\pi r^2 \gamma_{ow} (1 - |\cos\theta|)^2 \tag{2.8}$$

From this equation, we can see that the attachment energy is maximized if $\cos\theta = 0$, which corresponds to a contact angle of 90° and thus the particle being neutrally wetting. Furthermore, the attachment energy scales with the radius of the particle squared, which means that either large particles or a high oil-water interfacial tension is required.

2.1.3 Nanoparticle surface chemistry modification

As we have seen in the previous sections, we want to use particles that are neutrally wetting to increase the attachment energy, and so we can stabilize curved interfaces. The particles that are used in this work are Ludox TMA particles that are made of silica with aluminium inclusions. The surface of these particles is covered with hydrophilic hydroxyl groups that can become deprotonated and thus negatively charged depending on the pH. This means that the surface chemistry has to be adapted to make it neutrally wetting.
The surface chemistry is changed by introducing the surfactant hexadecyltrimethylammonium bromide (CTAB) into the particle dispersion. This surfactant has a positively charged head group that can adsorb to negatively charged deprotonated hydroxyl groups on the particle surface, and has a 16 long carbon chain as a tail that makes the particle is adsorbs to more hydrophobic. By balancing the surface charge using pH, and the CTAB adsorption via its concentration, neutrally wetting particles can be prepared.

2.1.4 Bijel synthesis

To make a bijel, a homogeneous precursor mixture of oil, water, and particles needs to undergo a change, so the liquids go from miscible to immiscible and phase separate through spinodal decomposition. There are several methods of inducing this change that have resulted in bijels. However, it is first helpful to further understand spinodal decomposition.
Spinodal decomposition is the mechanism of spontaneous separation of a single phase into two, which can happen when nucleation is bypassed[24]. Nucleation is bypassed when the composition of the mixture when phase separation starts is unstable instead of metastable, as a metastable system requires overcoming a nucleation barrier and thus phase separates via nucleation and growth. A mixture becomes unstable when crossing through the critical point of a binary or ternary phase diagram. As there is no nucleation required for a mixture demixing close to this point, the decomposition of the two phases starts throughout the whole volume, which generates a fine highly connected network that coarsens as the interfacial area is minimized.
The first method that was used to successfully create a bijel is by thermal quenching[15, 25]. In this process, a mixture of two liquids that has a lower critical solution temperature is heated to above this temperature, which causes the two to become immiscible and undergo spinodal decomposition. This amount of binary mixtures that can be used for this is however very low, and they are made in batch processes, which limits their applications. Further methods include non-solvent induced phase separation (NIPS), where demixing is induced by the diffusion of a non-solvent into and a solvent out of a mixture, which is used mostly for polymers, vaporization-induced phase separation (VIPS), where phase separation is induced by evaporation of a cosolvent in air, and Solvent Transfer Induced Phase Separation (STrIPS), which is used in this work.

As the name suggests, in STrIPS, phase separation is induced by solvent transfer, which means that a cosolvent diffuses from the precursor mixture into a continuous phase, which changes the composition from the miscible to the immiscible region. In this work, the oil used is 1,4-Butanediol diacrylate (BDA) which is made miscible with water by adding ethanol. When this is extruded into water the ethanol diffuses out and phase separation starts.
To further understand this process, it is insightful to track the change of composition in the ternary phase diagram in Figure 2.5. We start at a precursor dispersion composition close to the critical point but still in the miscible region of the phase diagram marked *i*.

If this precursor is extruded in water, and thus ethanol diffusion starts, the composition moves through the critical point and decompositions spinodally into an oil-rich and a water-rich phase marked *ii* and *iii* respectively. As more ethanol diffuses out, the oil and water rich phases separate further in a secondary phase separation step, which is further from the critical point and proceeds via nucleation and growth. After enough time has passed, all ethanol will have diffused out, and the oil- and water-rich phases will be solely oil or water.
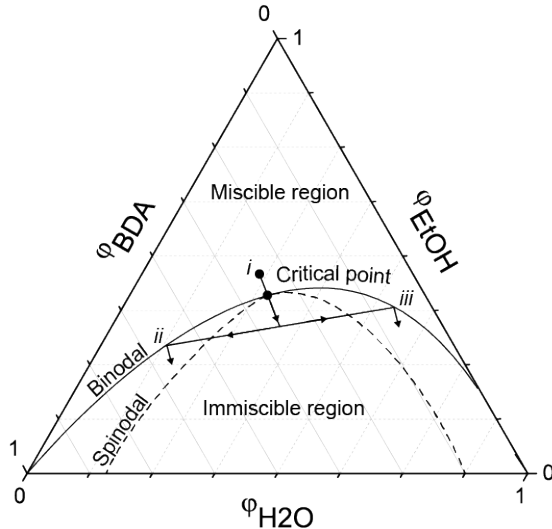

Figure 2.5: Ternary phase diagram of BDA-EtOH-water, with an approximate pathway of STrIPS. The initial composition is marked as *i*, which undergoes phase separation in an oil-rich phase (*ii*), and a water-rich phase (*iii*). Ternary phase diagram is adapted from Siegel et al.[11].

The separation of the phases leads to the creation of an interface to which the particles in the dispersion start adsorbing. As we saw in section 2.1.2.1 this is driven by the interfacial tension between the oil and water phase. This interfacial tension increases with decreasing solvent concentration, and thus particles attach to the interface stronger as STrIPS progresses[10]. However, this also means that at higher solvent concentrations the particles are not yet irreversibly attached, and the structure can grow more coarse as the interfacial area is minimized. This effect is often seen in bijels and result in a fine structure at the bijel surface which grows coarser when going deeper.
Marangoni flow is a surface tension driven flow that is the cause for so-called "tears of wine" and coffee circles[26]. This flow is caused by gradient in surface tension and flows from low to high surface tension. It is hypothesized that this can occur in the STrIPS process as the interfacial tension is high at the surface, where the ethanol concentration is lower, and the interfacial tension if lower deeper into the bijel.

2.2   Membrane fabrication

Having build a better understanding of how bijels are made, we now look at how we can use bijels as a template for solid membranes, and how we can fabricate these continuously. First, we need to know what membrane features influence their performance in filtration, then we need to look at the roll-to-roll production method which is used to coat precursor dispersion on a flexible substrate, next we explain how the wetting of the precursor on the substrate influences the coating process, and finally we see how to photopolymerize BDA to obtain a solid polymer scaffold.
From literature, we know that the selectivity is affected by the pore size of the largest pores. Since even if the mean pore size is small and would results in a high selectivity, there can still be a large flux with low selectivity through the largest pores[27]. Furthermore, there is

always a trade-off between selectivity and throughput, as a small pore size might increase the selectivity, but will also constrain flow[28]. Both of these factors are optimized by having a narrow pore size distribution, as then the amount of pores that either restrict flow but have less influence on selectivity is minimized. Another trade-off is between having an open interior that facilitates high flux, and mechanical strength resulting from an interior filled with a symmetric structure. Lastly, high surface areas can be required, especially when functionalized particles are incorporated in the membrane.

2.2.1 Roll-to-roll manufacturing

Roll-to-roll processing is a manufacturing technique that is used in industrial scale manufacturing, as it can be used to make flexible products with a high throughput. The technique aims to process a starting roll of substrate into a roll of product by applying production steps onto the substrate. These often include coating steps followed by post-processing steps such as lithography. This production method is used in a variety of processes such as the manufacturing of polymer solar cells[29], electronic device[30], and organic LEDs[31].

In this project, a relatively facile roll-to-roll process is used, consisting of a coating and a photopolymerisation step. The slot-die method is used to coat the precursor onto the substrate, this method pumps precursor through a thin slit nozzle, which is positioned in contact with the substrate[32]. For this coating method, it is important that the precursor wets the substrate, and that it does not wet the nozzle to prevent clogging. The wetting on the substrate and modification of glass nozzle surface are discussed in the following sections.

2.2.2 Substrate wetting

Wetting of a droplet on a substrate in a continuous phase of either air or another liquid is governed by three-phase contact angle θ (equation 2.9. The contact angle is a function of the interfacial tensions of the substrate-droplet interface ($\gamma_s d$), the droplet-continuous phase ($\gamma_d c$), and the substrate-continuous phase (γ_{sc}).

$$\cos\theta = \frac{\gamma_{sc} - \gamma_{sd}}{\gamma_{dc}} \tag{2.9}$$

A droplet wets the surface if the contact angle is lower than 90° and it dewets the surface when the contact angle is above 90°. This means that in the case of a coating process, where we want the droplet to wet the surface, $\gamma_{sc} - \gamma_{sd}$ must be positive, and thus interfacial tension between the surface and continuous phase must be higher than that of the continuous phase and the substrate[32].

2.2.3 Nozzle modification

To prevent a precursor wetting a nozzle and thus sticking to it, its surface can be modified to alter the interfacial tension between it and the precursor. In the case of a glass nozzle, this can be done using the polyelectrolyte poly(diallyldimethylammonium chloride) (pDADMAC). The adsorption of the polyelectrolyte onto the surface is partially driven by electrostatic interactions between the positively charged groups of the polyelectrolyte with the negative charges of silanol groups of the glass, and partially driven by an entropy gain from the release of salt ions[33]. This coating negates the negative charges of the silanol groups, making the surface more hydrophobic, although there can still be exposed positively charged groups from the polyelectrolyte on the surface. The coating prevents the adsorption of CTA^+ molecules.

2.2.4 Acrylate photopolymerisation

Photopolymerisation is an ideal option for polymerization in a continuous process such as roll-to-roll fabrication, as a photo-initiator can be dissolved in the monomer oil and the polymerization started via UV irradiation. As the photo-initiator is homogeneously distributed

through the monomer, polymerization is started throughout the whole oil phase and a highly cross-linked polymer can be achieved in seconds[34].

Diacrylates like 1,4-Butanediol diacrylate (BDA) work well as monomers for photopolymerisation due to their fast reaction rate though a radical polymerization mechanism[35], and due to the mechanical strength of the resulting cross-linked polymer. The radical polymerization is initiated using photo-initiator 2-hydroxy-2-methylpropiophenone (HMPP). Under UV-irradiation HMPP is cleaved into a benzoyl radical and a 2-hydroxyl-2-propyl, the radical receives a π electron from a double bond of BDA, and thus creates a free radical in BDA which can propagate the reaction to further BDA monomers (Figure 2.6).
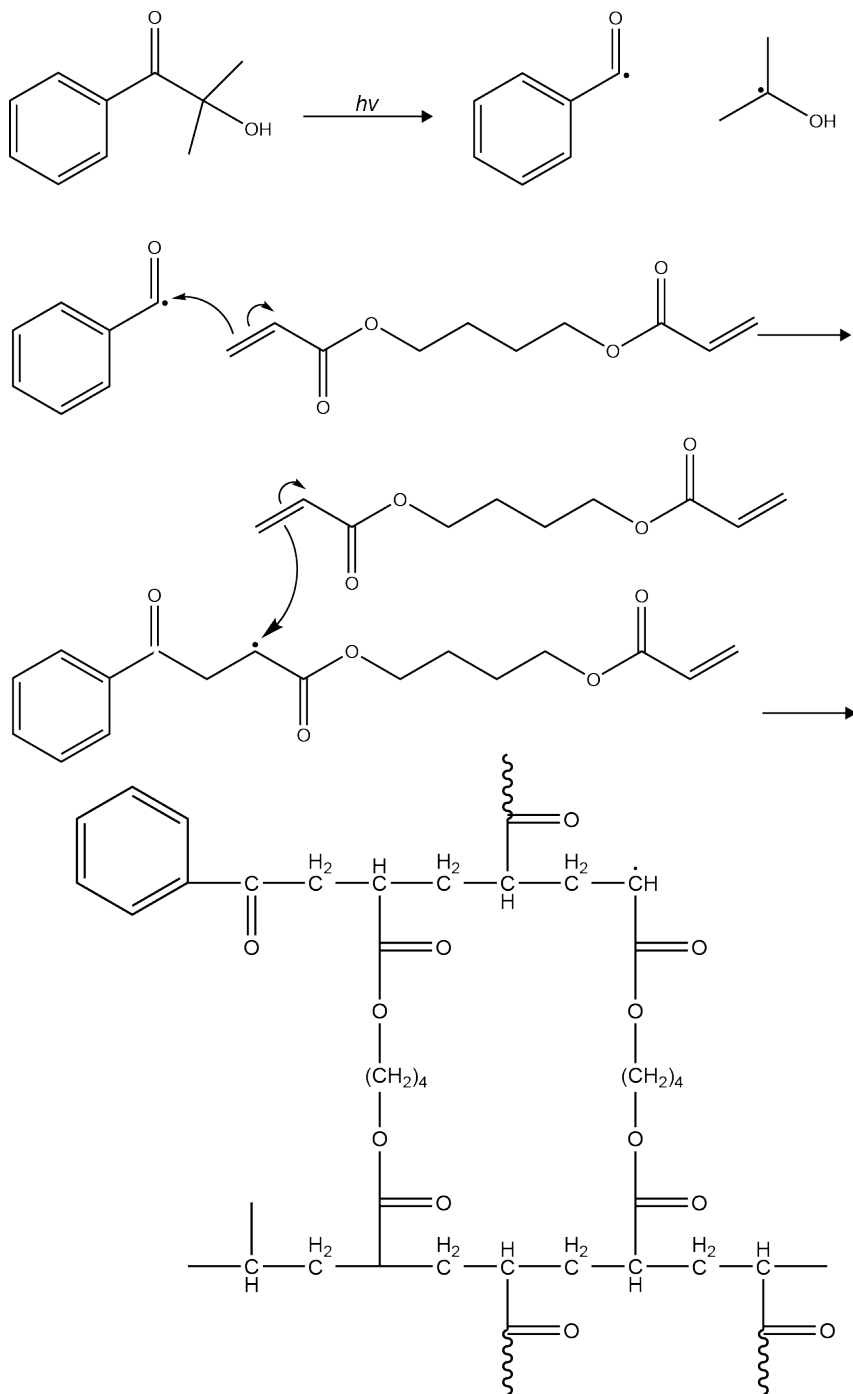

Figure 2.6: Reaction mechanism of photopolymerisation of BDA in the presence of HMPP[34, 35].

Materials and methods

3.1 Materials and preparation

3.1.1 Materials

Table 3.1 provides an overview of the chemicals and materials used for the experiments and are grouped according to their application in the present work.

Table 3.1: Matrials used in experiments including purity grade, application, and supplier.

Materials	Purity	Application	Supplier
1,4-Butanediol diacrylate (BDA)	Technical grade	Monomeric oil	ChemCruz
2-Hydroxy-2-methylpropiophenone (HMPP)	97 %	Photoinitiator	Sigma Aldrich
Ethanol (EtOH)	100 %	Solvent	Supelco
Hexadecyltrimethylammonium bromide (CTAB)	$\geq 99\,\%$	Surfactant	Sigma Life Science
Ludox® TMA	34 wt. % in H_2O	Nanoparticles	Grace
Sodium chloride (NaCl)	Analysis grade	Salt	Supelco
Polyethylene terephthalate (PET) window foil	-	Substrate	Reflectif
Epoxy adhesive	-	Nozzle construction	Liqui Moly
Optical adhesive	-	Nozzle construction	Norland
Teflon tubing 1.3 mm ID	-	Nozzle construction	AlphaWire
Microscopy slide 22 x 22 mm #1	-	Nozzle construction	Menzel-Gläser
Poly(diallyldimethylammonium chloride) (PDADMAC)	20 wt. % in H_2O	Polyelectrolyte	Aldrich
Diethyl Phthalate (DEP)	99 %	Index matching	Acros organics
Nile Red	Microscopy grade	Fluorescent dye	Sigma
Rhodamine 110 chloride	$\geq 97\,\%$	Fluorescent dye	Chemodex
Hydrochloric acid (HCl)	37 % in H_2O	Acid	Acros Organics
Sodiumhydroxide (NaOH)	99 %	Base	Emsure
Dichloromethane (DCM)	$\geq 99.9\,\%$	Solvent	Biosolve
Trifluoroactetic acid (TCA)	$\geq 99.9\,\%$	Solvent	Honeywell | Fluka
Tertrahydrofuran (THF)	$\geq 99.8\,\%$	Solvent	Biosolve
Polylactic acid (PLA)	-	3D print plastic	Dremel

3.1.2 Nanoparticle preparation

3.1.2.1 Nanoparticle dispersion in water

For preparation of precursor dispersions, the 34 wt.% Ludox TMA particle stock dispersion is concentrated by heating at 80°C on a heating plate (IKA) and weighing to calculate if the desired particle weight fraction (wt.%) of 45-50 wt.% is reached. After concentrating the particle dispersion, particle aggregates are removed via centrifugation at 3750 rpm for 10 minutes (Beckman Coulter Allegra X-12R). The particle dispersion is dialysed overnight in 800 mL of MilliQ water containing 50 mM NaCl at pH 3. The particle weight fraction is determined by weighing 0.5 mL before and after evaporating the water on the heating plate.

The density is measured by weighing 1 mL of the concentrated dispersion using a calibrated pipette.

3.1.2.2 Nanoparticle dispersion in ethanol

Particles in ethanol are prepared by exchanging the solvent of the Ludox TMA stock dispersion from water to ethanol. The Ludox TMA stock is dialysed for 16 hours in 800 mL of ethanol, the ethanol is replaced after 8 hours. The bath is covered with aluminium foil to avoid ethanol evaporation. Removal of particle aggregates and determination of the weight fraction and density are performed in the same way as described in the previous section.

3.1.3 Precursor dispersion preparation

The compositions of the four precursor dispersions that are used are shown in the ternary phase diagram in Figure 3.1. The liquid precursor compositions are chosen close to and off to higher BDA content from the critical point of the BDA/ethanol/water phase diagram to incorporate sufficient BDA, which serves as scaffold substance for the membrane. For all precursor dispersions, the surfactant concentration ranges from 15 to 84 mM and the nanoparticle mass fractions range from 110 to 274 mg/g (Table 3.1). Both the nanoparticle mass fraction and the CTAB concentration are in respect to the complete volume of precursor dispersion including the solvent.
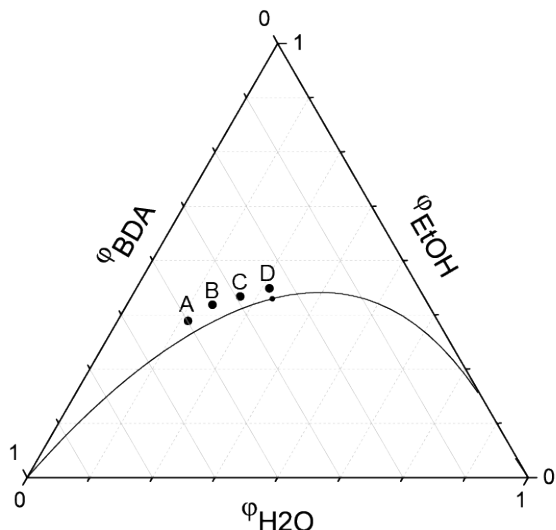
Liquid volume fraction	A	B	C	D
ϕ_{BDA}	0.500	0.433	0.367	0.303
ϕ_{H_2O}	0.140	0.168	0.215	0.270
ϕ_{EtOH}	0.360	0.399	0.418	0.427
Particle mass fraction (mg/g)	110 - 274			
C_{CTAB}(mM)	15.0 - 84.0			

Figure 3.1: Ternary phase diagram for BDA/ethanol/water with precursor compositions labelled as A, B, C, and D. Liquid volume fractions are expressed by φ.

The dispersions are prepared by mixing Ludox TMA nanoparticles dispersed in ethanol and water, CTAB, EtOH, BDA and demineralized water. BDA includes 5 vol. % of photoinitiator HMPP as well as a small amount of the fluorescent dye Nile Red for confocal imaging. The dispersions are homogenized using a vortex mixer (Scientific Industries) and sonication bath (Branson 1800).

3.2 Membrane fabrication

In the present study, the membrane fabrication is performed using a flexible support substrate in a roll-to-roll process. The processing steps needed to fabricate bijel templated membranes are the following: first, the precursor dispersion is deposited as thin film onto the substrate. Second, the precursor film deposited onto the substrate is pulled through a water bath to induce solvent diffusion out of the precursor to initiate the structure formation process. Last, the BDA is photo-polymerized by irradiation with a UV-lamp to form a

crosslinked membrane scaffold.

The coating machine is a prototype roll-to-roll Lego machine adapted from a design previously made in the physical and colloid chemistry group [13](Figure 3.2). The details of how the machine works are described in the following sections.
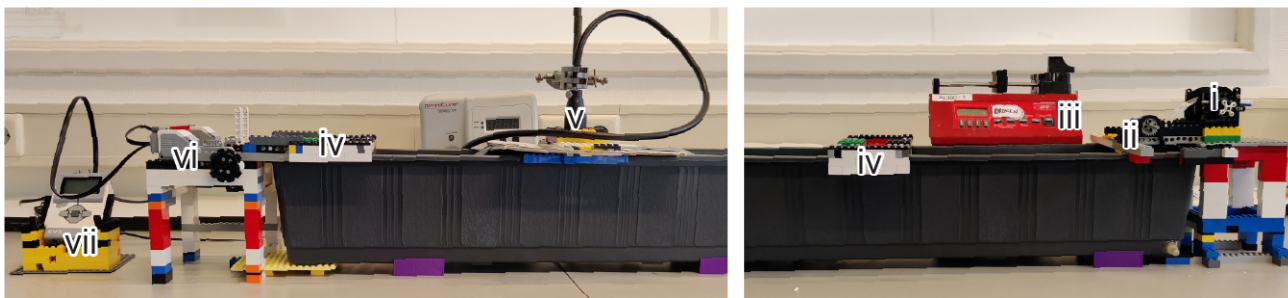

Figure 3.2: Photograph of the Lego coating machine with from right to left (i) the substrate stock roll (ii) the deposition area and nozzle holder (iii) the syringe pump (iv) the support and alignment rollers (v) the UV-lamp (vi) the Lego motors and product roll (vii) the Mindstorms control unit.

3.2.1 Substrate and drive

3.2.1.1 Substrate

The substrate is a flexible PET window foil. This foil is a composite material made of silicone between two layers of PET and is purchased in sheets of 1.52 x 5 m. It is cut to strips of 38 mm in width, taped together with scotch tape, and collected on a 3D printed substrate stock roll.

3.2.1.2 Drive

The substrate is pulled by two Lego motors which are connected to the axle of the product roll. The speed of the substrate is controlled by the Lego Mindstorms software and is set as a percentage of the maximum motor power, which is converted to substrate speed via the internal tachometer of the motors (Figure 3.3). Unless stated otherwise the motors run at 20 % of their maximum which corresponds to a substrate speed of 5 cm/s.
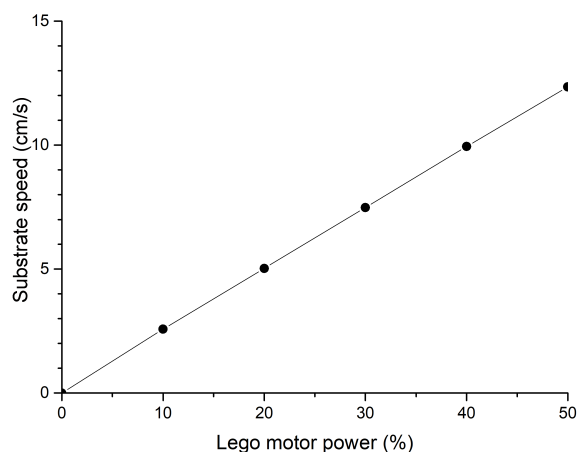

Figure 3.3: Speed of the substrate as a function of power percentage of the Lego motors.

3.2.1.3 Alignment and tension

Maintaining stability and preventing lateral movement of the substrate is important during coating and membrane structure formation. The membrane is kept straight and tight by the guiding rollers which are placed at a constant distance from the edge of the water bath (Figure 3.4(a)). The substrate is kept under tension by applying a drag force onto the axle of the stock roll. This is done by putting a rubber Lego wheel onto the axle, which is deformed by pressing a Lego plate into the wheel. This deformation causes a force which opposes rotation as soon as the axle is turned (Figure 3.4(b) and (c)).
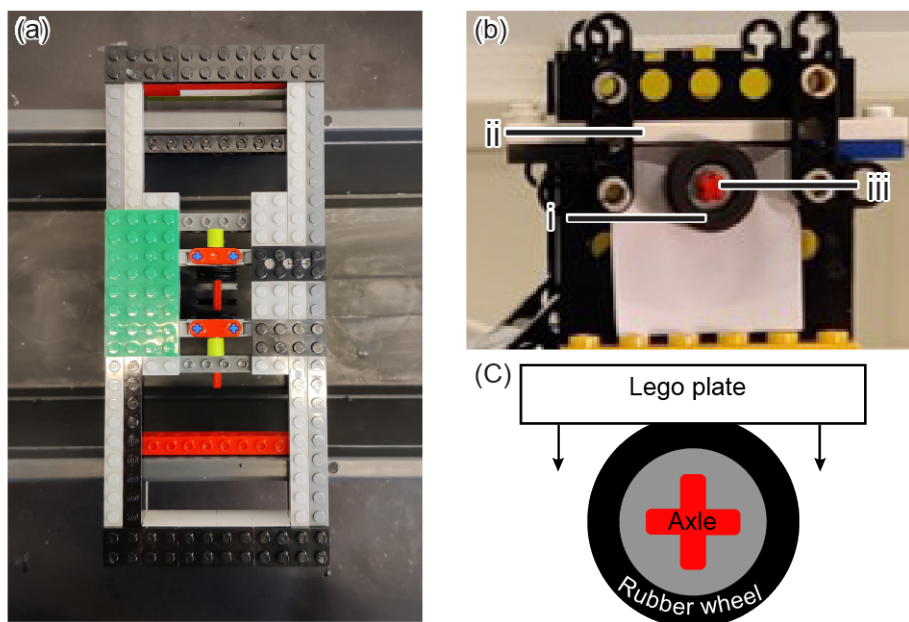

Figure 3.4: Photographs of (a) the alignment system, and (b) the tensioning system where the rubber wheel (i) is pressed into plate (ii), the wheel is connected to the substrate roll by axle (iii). (c) schematic of the Lego wheel being deformed by pressing a Lego plate into it, which causes drag on the axle.

3.2.2 Coating

3.2.2.1 Nozzle

The precursor dispersion in deposited onto the PET substrate using a rectangular glass nozzle with dimensions of 10 mm in width and 100 µm in heigth. The flow is driven by a NE-300 Just Infusion syringe pump (New Era). The nozzle is made by gluing two 6 mm x 22 mm x 100 µm pieces of microscopy slide (Menzel-Gläser) in between two 22 mm x 22 mm x 100 µm slides (Figure 3.5). The nozzle orifice is formed by the missing part in between the two pieces of the centre slide and is 10 mm wide. The slides are glued together, and then connected to the pump using 1.3 mm inner diameter PTFE tubing. The tubing is attached to the nozzle by making an incision along its length, inserting the nozzle, and gluing the nozzle in place.

The nozzle is coated with Poly(diallyldimethylammonium chloride) (PDADMAC) to prevent adhesion of the precursor dispersion. This is done by leaving a 0.2 wt.% PDADMAC solution containing 0.5 M NaCl in the nozzle for 5 minutes, after which it is washed with ethanol and dried.
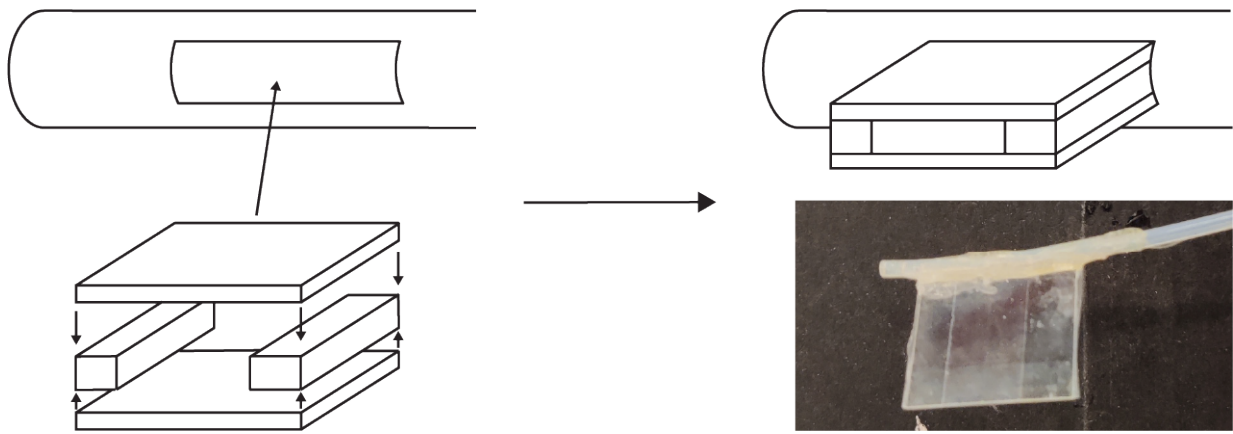
Figure 3.5: Schematic of assembly of a nozzle, and photograph of a finished nozzle. Scale bar is 10 mm.

3.2.2.2 Deposition

The schematic of the coating machine in Figure 3.6 shows how the substrate is entering the water bath directly from the stock roll. Right after, it is guided through a series of rollers to the nozzle, where the precursor dispersion is deposited. This is in between two rollers which keep the substrate in position during deposition. The nozzle is held in place by a 3D printed holder that presses it into the substrate, so contact is maintained (Figure 3.7). The angle between the nozzle and the substrate influences the uniformity of the coating on the PET substrate, and has been determined to be optimal at 55°in respect to the substrate[13]. This angle is controlled by rotating a gear that is attached via the nozzle holder, this gear is connected to a gear in the structure via a chain system which is can be locked in place during deposition. This ensures continuous contact of nozzle and substrate.
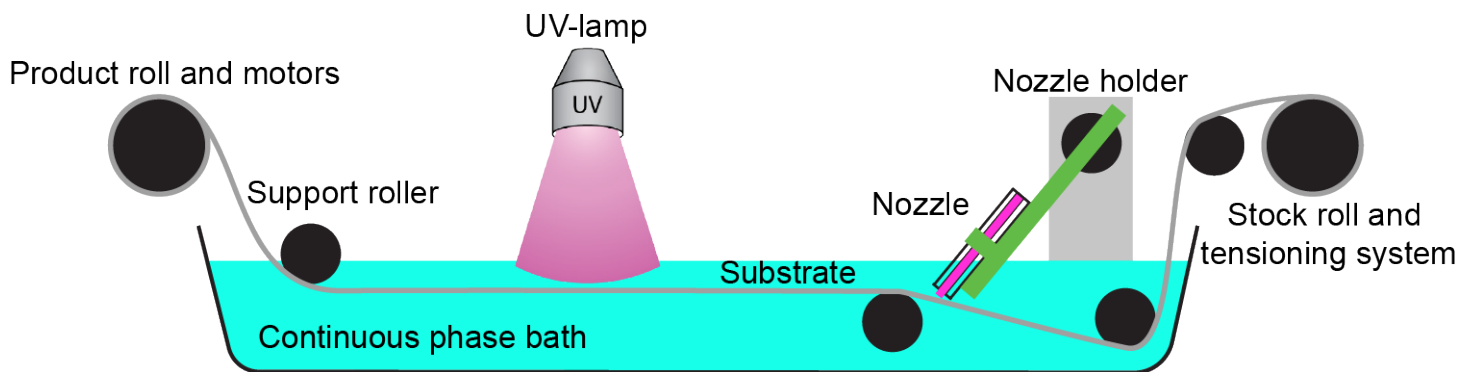

Figure 3.6: Schematic of the coating machine.

3.2.3 UV polymerization

The UV lamp used for UV-polymerization is an Omnicure s1500 UV lamp (Excelitas technologies). Its beam is kept focused by an aluminium foil cylinder which extends till 1 cm above the substrate to avoid premature polymerization (Figure 3.7). The lamp is placed at the end of the bath at a distance of 150 cm to the deposition nozzle, which corresponds to a travel time of 30 seconds between nozzle and polymerization at the standard substrate speed of 5 cm/s. This distance can be varied from 3 to 150 cm, which is used to change the duration that STrIPS has to take place before membrane is solidified.
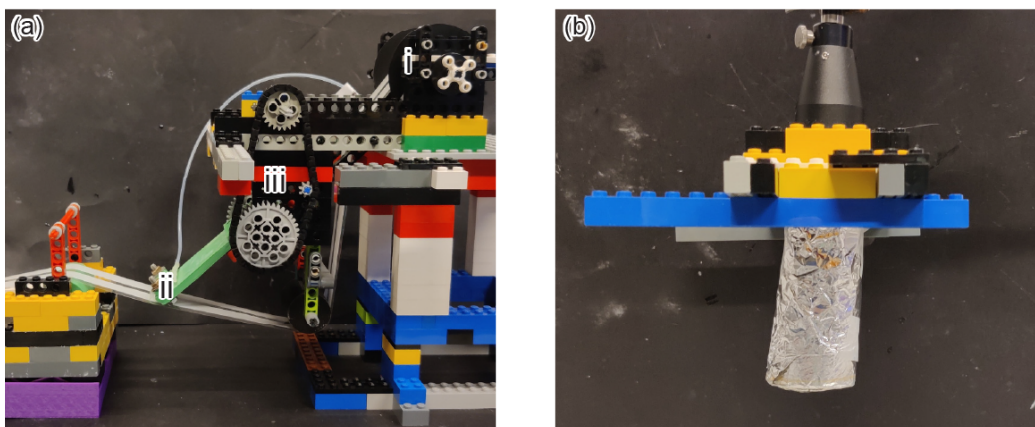

Figure 3.7: Photo of (a) the precursor dispersion deposition, with (i) the substrate roll, (ii) the deposition nozzle, and (iii) gear and chain system that rotates the nozzle into place and locks its position. (b) UV-lamp housed into aluminium foil to avoid UV scattering.

3.3 Wetting studies

The wetting of the PET substrate by the precursor dispersions influences the spreading during precursor deposition. Therefore, the contact angles between the PET substrate and precursor dispersions A-D without particles and a given CTAB concentration of 50 mM are evaluated. This is done on the OCA 15 plus contact analysis system (Dataphysics) using the sessile droplet, inverted sessile droplet, and advancing contact angle methods. This system records droplets dispensed in a liquid by a syringe pump. From the resulting movies the contact angle is measured.

Three methods are employed by depositing a droplet of precursor dispersion onto the substrate. For the sessile droplet method, the droplet is deposited directly onto the substrate and does not stay in contact with the needle. This is the same for the inverted sessile droplet method, and it is employed for measuring the contact angle of a bubble in liquid and liquid in liquid when the density of the droplet is lower than the liquid it is measured in. For the advancing contact angle, precursor is continuously dispensed through the needle without detachment.

During membrane production, precursor dispersion is deposited on the substrate in water as a continuous phase, this causes the wetting behaviour to be different from in air. This influence is studied by changing the composition of the continuous phase using surfactant and solvent. Contact angles are measured in (i) air, (ii) water of pH 3, (iii) water of pH 3 with 5 mM CTAB, and water of pH 3 with (iv) 5, (v) 10, or (vi), 20 vol. % ethanol, respectively. Due to the relative densities of the precursors and the continuous phases, the contact angle of precursor A on the substrate is measured at using the sessile drop method and contact angles of precursor B-D are measured using the inverted sessile drop method.

Sessile drop measurements are performed in a rectangular container into which a support table is placed which has a 10 x 10 mm piece of PET substrate glued to it (Figure 3.8(a)).

The dispersion is deposited from the top via the syringe pump of the contact angle measurement system. For the inverted sessile drop method, the support table is flipped upside down and a second support holding a needle connected to the syringe pump is placed under it(3.8(b)). The measurements in air are performed by depositing the precursor dispersion onto a microscopy slide lined with a 10 x 10 mm piece of PET substrate.

The contact angles are measured by recording the deposition of the precursor dispersion on the PET substrate using the camera of the contact angle analysis system at 25 frames per second. For the measurements in air, the 5-6 µL of precursor is deposited at 10 µL/s. For the measurements in all the continuous phases, 5-6 µL is deposited at 15 µL/s.

The analysis of the recorded movie is done using the contact angle plugin on ImageJ. The baseline is determined by placing two points on the water-substrate-precursor interface. Then three to five points are placed manually on the precursor/water interface. The plugin performs an elliptical fit through these points and outputs the contact angles.
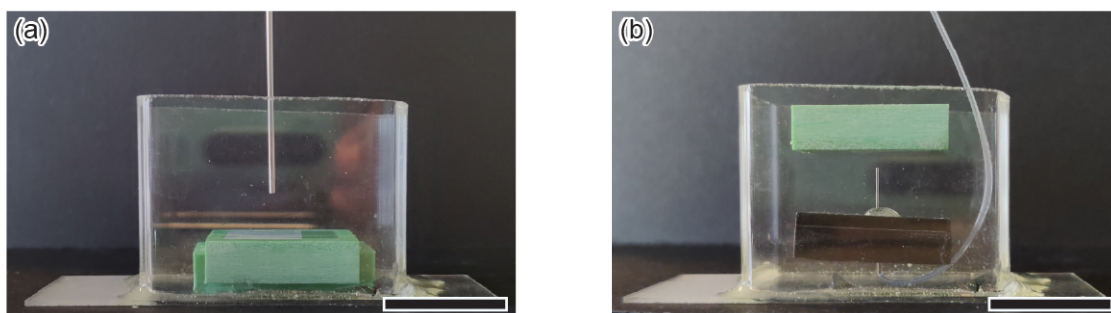

Figure 3.8: Containers used for contact angle analysis in the continuous phase for (a) right side up, and (b) for inverted measurements. Scale bars are 20mm.

3.4 Substrate dissolution

One centimetre of dry membrane that is attached to the substrate is submerged into 10 mL of DCM, THF, or TCA, respectively, overnight. After this, the substrate is dissolved, and the membrane is taken out of the solvent using a pair of tweezers.

3.5 Characterization

3.5.1 Scanning electron microscopy(SEM)

3.5.1.1 Sample preparation and measurement

Dried membranes are prepared for SEM analysis by cutting across the length to expose the cross-section. Four pieces of membrane are stuck to a support, two pieces have the cross-section exposed, one piece has the top surface exposed, and for one piece the bottom surface is exposed. The four exposed sides are all imaged three times, once at an overview with 1000x zoom, and two zoomed in images at 2500x zoom. The SEM images are acquired on a Phenom ProX electron microscope at an operating voltage of 10 kV, analysis is done in ImageJ.

3.5.1.2 Data analysis

The thickness of membranes is measured in ImageJ by analysing the cross-sections of the membranes. This is done by first rotating the image till the top edge is horizontal. Then the thickness is measured by aligning the top of a rectangular selection and measuring the height at the minimum and maximum thickness of the image.

Pore size analysis is performed on SEM images of the top of the membranes at 5000x zoom.

The images are divided into a 5x5 grid and for each grid square the largest pore size is measured. The pore size is reported as the diameter of the smallest circle that fits around the pore. The standard deviation is taken over these 25 pores.

3.5.2 Laser Scanning Confocal Microscopy (LSCM)

3.5.2.1 Sample preparation and measurement

The membranes are prepared for confocal analysis by first labelling the silica nanoparticles with Rhodamine 110 chloride. To this end, CTAB is removed by washing twice with a 50/50 v/v EtOH/1 M HCl solution, after which the particles are stained for 1 hour using a saturated solution of Rhodamine 110 chloride in 0.1 M NaOH. The membrane is then washed twice with MilliQ water to remove the Rhodamine. Finally, the poly-BDA membrane dried completely, so it can be made optically transparent by refractive index matching with DEP. The membrane is then put in between two microscopy slides to be measured on a Nikon Eclipse Ti-U, Leica Stellaris 5 confocal microscope.
Nile Red and rhodamine 110 are excited with 488 nm and 561 nm lasers respectively, with the fluorescent detection ranges at 500-550 nm and 600-700 nm respectively. The three-dimensional structure is probed by scanning the fluorescence at different focal depths and making a z-stack. Z-stacks are measured at a 1024x1024 pixel resolution under 2x zoom and with a z-step of 0.33 µm. The z-stack is converted into a 3D structure by extrapolating between the different layers using the 3D viewer plugin of ImageJ. The procedure for this is to first set the brightness and contrast, then to merge the oil and particle channels, and then converting the stack to RGB. By running the 3D viewer plugin with a resampling factor of 1, the stack is converted to a 3D reconstruction.

3.5.2.2 Data analysis

The interfacial area and the volume fractions of oil and water channels are measured using ImageJ. For these measurements, only the fluorescence of Nile Red (500-550 nm) is used. The whole z-stack is analysed, so the oil volume fraction can be determined by counting the area of all pixels that give signal for Nile Red and multiplying with the step size in the z-direction. The same is done for the interfacial area after the outline of the interface is determined. This is done in ImageJ via the following steps, an example analysis for a single image is shown in Figure 3.9. First, all images are binarized with an automatic threshold set by the "make binary" processing step in imageJ for all individual images. Second, the despeckle function is run to remove small patches of pixels that are caused by noise. Now, the area of black pixels is measured and used to calculate oil volume fraction. Next the outline and skeletonize commands are applied. This first provides an outline of all surfaces and then ensures the line is one pixel thick. The outline command counts the edge of the image as an outline as well, while this does not correspond to surface area, so the outer line of pixels is removed before measuring the area again.
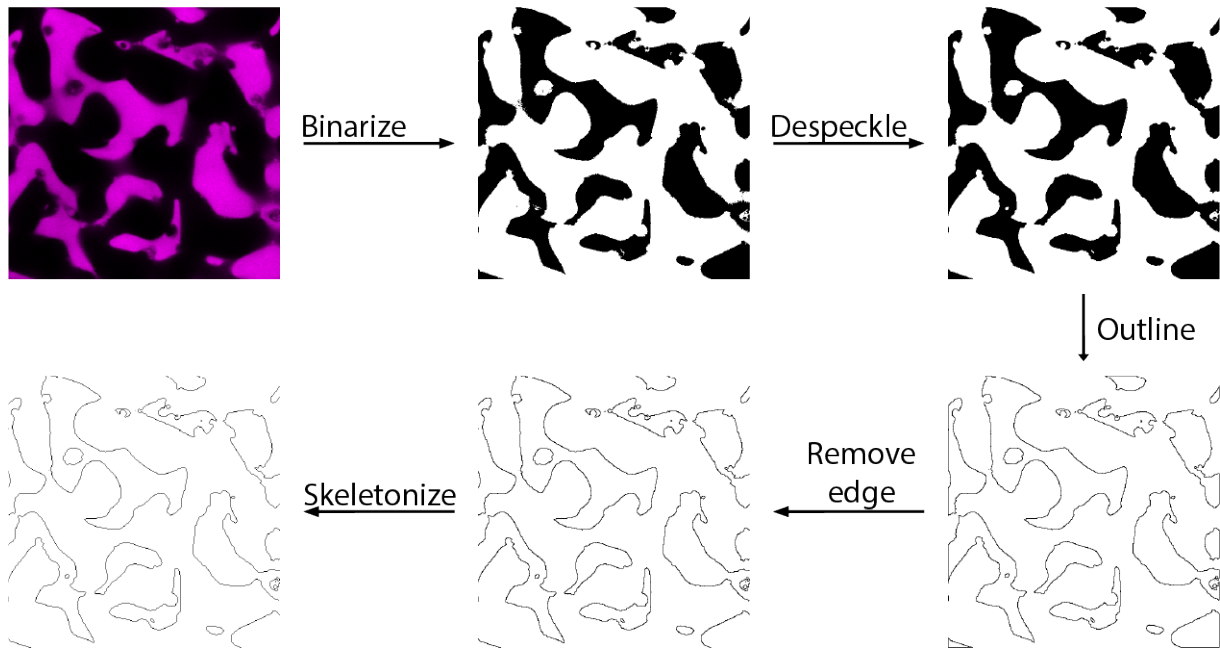
Figure 3.9: Analysis of the oil volume fraction and surface area. The black area is measured after the despeckle and the skeletonize step.

3.6 3D printing

The 3D models for printed parts are designed using the Autodesk Inventor software. The models are converted to a printable toolpath by the Dremel 3D idea builder software and printed on the Dremel DigiLab 3D45 printer in PLA filament.

3.7 COMSOL simulation

A COMSOL Multiphysics (software version 5.6) solvent diffusion simulation is used to simulate the ethanol diffusion out of a deposited film of precursor. The Transport of Diluted Species (TDS) module of COMSOL is used to simulate the concentration change over time of ethanol. The film of precursor is modelled as a 2D cross-section of 10 mm wide and 100 µm high, which connects to 10 cm of continuous phase. The initial concentration of ethanol inside the film is calculated from the volume fractions in the precursor, and is 7317.5 mol/m^3, the initial ethanol concentration in the continuous phase is set to 0. The diffusion coefficient was set to that of ethanol in water, which was taken from literature, and is plotted in Figure 3.10[36]. The membrane surface is simulated as a diffusion barrier of 10 µm thick that starts with the same diffusion coefficient as in the bulk, and decreases linearly to 30% of that within 0.2 seconds.
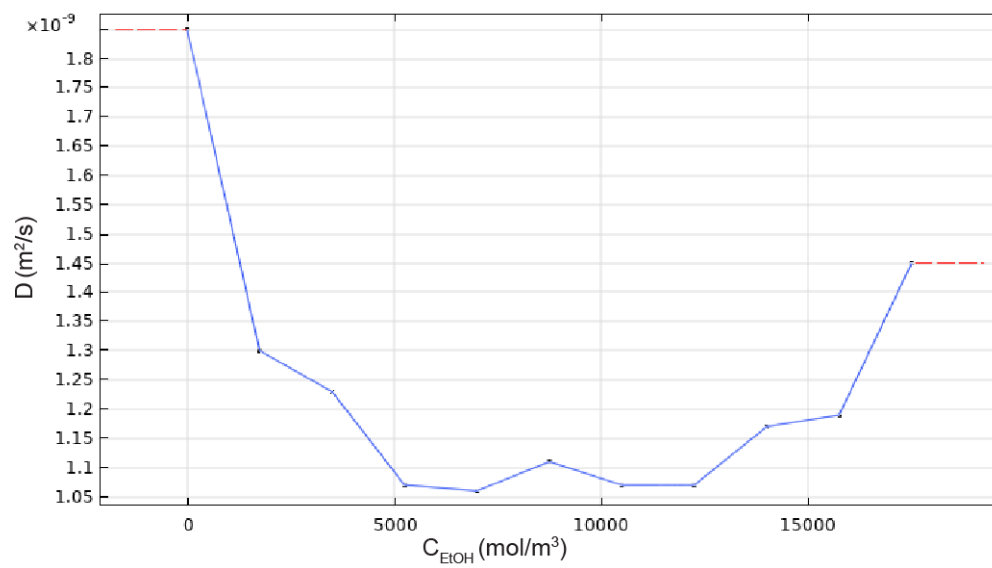
Figure 3.10: Diffusion coefficient of ethanol in water as a function of concentration[36].

Results and discussion

This chapter discusses the results of this work, and builds an understanding of the roll-to-roll production process and the structure of the resulting membranes. The aim of the chapter is to answer the question if we can continuously produce thin-film bijel-templated membranes with a controlled structure, and understand the process of their formation. To this end, we will look at a previous design of a roll-to-roll coating machine and how it is adapted to improve the reproducibility. Then the structure of the membranes is discussed, and it is shown how the structure is influenced by the composition of the precursor dispersion. After having looked into structural dependencies, we will see at how these structures form, which is done by polymerization of the membranes at different time steps during phase separation. This progression is then linked to simulations. Next, we will investigate how the deposition of the precursor is influenced by the wetting of precursor dispersions on the substrate. Finally, the homogeneity in membrane thickness is discussed and a formula to predict this is presented.

4.1 Membrane production

In previous work by G. Athanasiou a Lego roll-to-roll coating machine prototype has been designed that is capable of producing membranes via the STrIPS method[13]. The deposition method and the type of substrate have been optimized, which allows for control over thickness and continuous production. The membrane structure was not yet reproducible due to instability in the system and poor alignment of different parts.

The initial goal of this work was therefore to improve the reproducibility of the prototype Lego machine. This was achieved by rebuilding the prototype machine with a focus on minimizing the relative movement between the parts, and on substrate stability. Both the stability and rigidity have been improved by building the machine on the continuous phase bath (Figure 4.1), instead of having separate towers that are manually aligned as in the previous design. By aligning all the parts with the edge of the bath, the relative movement between the parts is decreased, resulting in an increase in stability. However, as the bath is a polypropylene (PP) plant pot with thin walls, it can bend under stress and thus not all movement is eliminated.
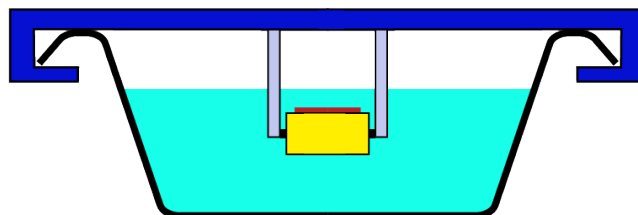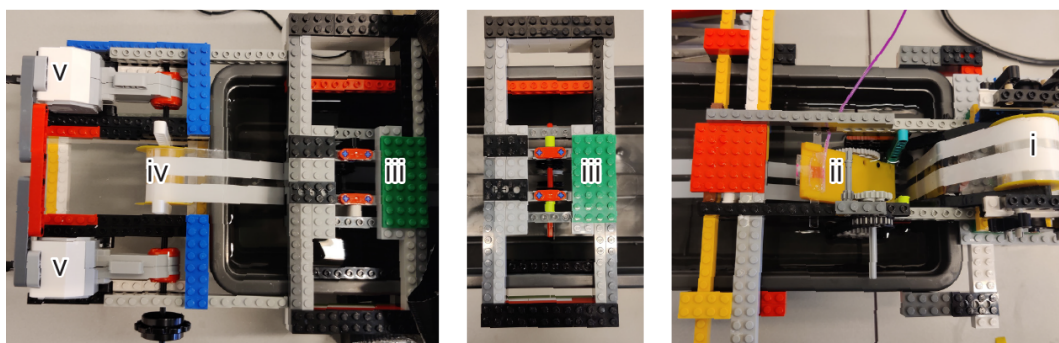
Figure 4.1: Photograph of Lego coating machine parts build around the continuous phase bath with (i) the product roll (ii) the deposition nozzle (iii) alignment roller (iv) the product roll (v) the Lego motors. And schematic of a part build onto the water bath, Lego support structure is shown in blue, support roller in yellow, and substrate in red.

By building the machine parts on the edges of the bath the problem of aligning separate parts is also addressed. As all parts are fitted to the edge of the bath, a constant distance between the rollers and the edge can be kept, which ensures all are in line with each other. All parts being in line prevents destabilization of the substrate by dragging against support structures.
The solution for increasing the stability of the substrate was to increase the tension on it. This keeps the substrate straight and tight, and prevents lateral movement. The tension is kept by pressing the substrate stock roll on a rubber Lego wheel that is attached to the axle, this deforms the wheel slightly and thus can enact a force opposing movement if the axle is turned.

Due to the increased robustness of the new machine design, the production process has higher reproducibility, and results in more uniform membranes (Figure 4.2 (a)). The process can still fail if the precursor dispersion does not adhere to the substrate, but instead drifts away into the continuous phase. It is hypothesized that this is caused by vibrations in the machine disrupting the contact between the nozzle and the substrate. To decrease vibrations, the support structure of the guiding rollers and the nozzle holder was strengthened. This did reduce, but not completely eliminate, the precursor drifting away in the production process.

After the polymerization, the substrate with membrane on it is cut away from the rolls of substrate, and left to dry. During drying, the membrane can either stay attached to the substrate (Figure 4.2 (b)), or detach while drying (Figure 4.2 (c)). The poly-BDA membranes shrink slightly while drying, which results in the membranes tearing or curling up upon detachment of the substrate. This could be an indication that the membranes are not completely homogeneous, as parts of different thickness will shrink at a different rate and therefore cause the distortion. This hypothesis will be further discussed in section 4.5. Having shown how the membrane production process was improved, the next section will discuss the wetting of precursor solutions on the substrate, as this is an important parameter in the coating process.

Figure 4.2: Poly-BDA membranes that have (a) stayed intact, (b) cracked, and (c) curled up during drying. Scale bar is 20 mm.

4.2 Wetting studies

The membranes should have straight edges and should be uniform in thickness across the width. Figure 4.3 (a) shows how the straightness of edges of membranes depends on the precursor composition used for the membrane. Frayed edges originate from the minimization of the surface area between precursor solution and continuous phase and is thus influenced by the wetting of the precursor on the substrate (Figure 4.3 (b)). As explained is section 2.2.2 this is influenced by the interaction between precursor dispersion, continuous phase, and substrate, which is investigated in the following section.
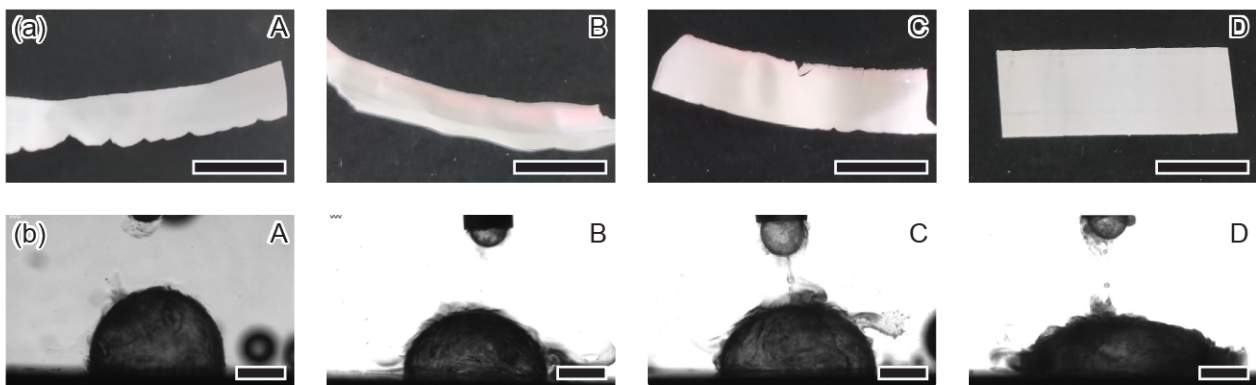

Figure 4.3: (a) Membranes produced with precursor dispersions A-D and (b) droplets of these precursors on the PET substrate in water. Scale bar is 10 mm in (a) and 1 mm in (b).

By depositing a droplet of precursor dispersion on the substrate, we can get an indication of its wetting behaviour. This is done using a contact analysis system that accurately deposits a chosen volume on a substrate and records the dispensing process. During membrane production, the precursor dispersion is deposited on the substrate in the continuous phase, and thus the wetting is investigated in the continuous phase. The wetting in air is measured as well, to investigate why precursors with a higher oil content seem to wet a hydrophobic substrate worse than lower oil content precursors.

The wetting can also be influenced by modifying the continuous phase, which is interesting for precursor compositions that do not wet the substrate but do result in a desired struc-
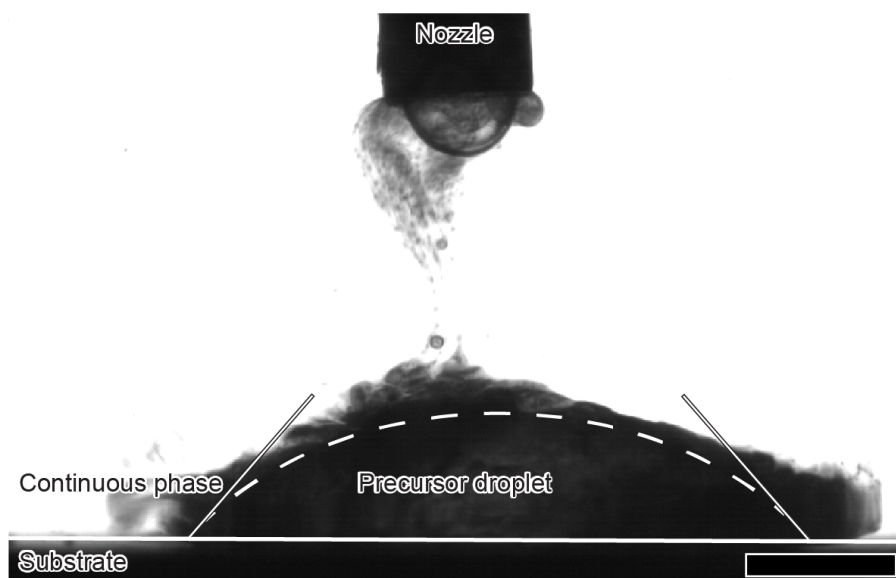
Figure 4.4: Precursor dispersion droplet during contact angle measurements with interference at the surface. The baseline, contact angles are shown in white lines, the interface is shown in a dashed line. Scale bar is 1.0 mm.

ture.Therefore, the wetting is tested in water of pH 3, water of pH 3 with 5 mM CTAB, and water of pH 3 with varying concentrations of ethanol.

The contact angle measurements in a continuous phase are complicated by ethanol diffusion and resulting phase separation. Due to these processes, the precursor composition, and thus the contact angle, will change over time. The measurements therefore result in a profile of the contact angle over time.

A second complication is optical interference around the droplet, which obscures the interface (Figure 4.4). This is caused by the ethanol diffusion, and by small oil droplets being ejected from the precursor duo to changes in the interfacial tension. Because the interface is obscured, automated analysis of the contact angle becomes impossible, therefore, analysis is done by hand.

The contact angles of precursors A-D with 50 mM CTAB, and without nanoparticles have been measured using sessile drop, and advancing contact angle methods. For the sessile drop method, a volume of precursor is deposited on the substrate and does not stay in contact with the deposition needle. For the advancing contact angle method, the deposition needle is positioned close to the substrate surface and the precursor is deposited continuously. Because of the continuous deposition, the droplet grows, and the contact line, where continuous phase, precursor, and substrate meet, moves, but the contact angle stays the same. Figure 4.5 shows the precursors and their densities. The precursors that have a higher density than water are done with the needle above the substrate. The contact angles of precursor with lower densities are measured inverted, where the droplet is deposited upwards and floats onto the substrate.

In sessile drop measurements, the precursor is deposited at a high volumetric flow rate, so it does not stick to the needle and is propelled towards the substrate. As it reaches the substrate, it needs to settle before the equilibrium contact angle is reached. During the time it takes to move to the substrate and settle, solvent diffusion is taking place and the contact angle is changing. This makes it challenging to choose when to start recording the contact angle, as starting too early means the deformation of the droplet will be measured, and starting too late means that the contact angle of a lower ethanol content precursor is measured. This means that the starting point is chosen manually, which introduces some variance.

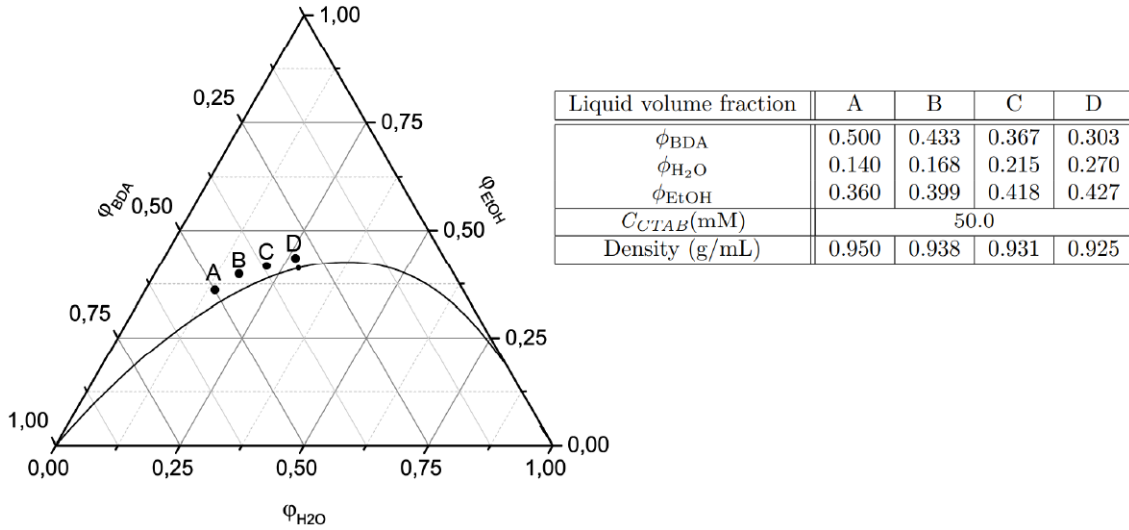| Liquid volume fraction	A	B	C	D
ϕ_{BDA}	0.500	0.433	0.367	0.303
ϕ_{H_2O}	0.140	0.168	0.215	0.270
ϕ_{EtOH}	0.360	0.399	0.418	0.427
C_{CTAB}(mM)	50.0			
Density (g/mL)	0.950	0.938	0.931	0.925

Figure 4.5: Ternary phase diagram for BDA/ethanol/water with precursor compositions labelled as A, B, C, and D. Liquid volume fractions are expressed by φ.

The advancing contact angle method was a proposed solution to the problems associated with the sessile drop method. Because precursor is deposited continuously, the precursor composition is replenished as ethanol diffuses out, which should limit the effect that the ethanol diffusion has on the contact angle. Secondly, as the precursor is deposited directly onto the substrate, there is no travel and settling time to take into account. This method does have a mayor disadvantage when measuring low contact angles. If the contact angle is too low, no droplet forms between the needle and the substrate, but instead all the ternary flows away. This makes it impossible to measure the contact angle.

Because measuring low contact angles with the advancing contact angle method did not work, it was not possible to compare precursors A-D using this method. Therefore, all results presented in the following sections are measured using the sessile drop method. The sessile drop method does not result in accurate contact angles due to the aforementioned problems, however it is still capable of providing insightful trends by comparison of the different precursors.

4.2.1 Continuous phase and air measurements

Figure 4.6 (a) shows how the contact angle changes over time for precursors A-D on the PET substrate in air, (c) shows the drop[lets at $t=0$. The contact angles in air start at 20-30°and decrease quickly till the precursors are almost completely wetting. The precursors are distinguishable by the initial contact angle and the slope with which the contact angle decreases over time. There is a trend visible going from precursor A-D where the initial contact angle increases, and the slope becomes less steep, indicating that the wetting decreases from A-D. As the PET substrate is hydrophobic, we hypothesize that the highest oil content precursors will have lower contact angles and thus wet the substrate better. The oil content increases going from precursor D to A, thus becoming more hydrophobic, which confirms the hypothesis. This trend does however oppose the observations made in Figure 4.3, where precursor A wetted the substrate better than precursor D.

Figure 4.6 (b) shows the contact angle over time of precursors A-D in water of pH 3, the droplets as they are at $t=0$ are shown in Figure 4.3 (b). These contact angles start at 80-100°and the decline over time is slower compared to the contact angles is air. These contact angles reveal the opposite trend compared to in air, and is consistent with observations during film production.

The large difference between the contact angles in air and water is caused by the differences in interfacial tensions. The big difference in contact angles between water and air stems
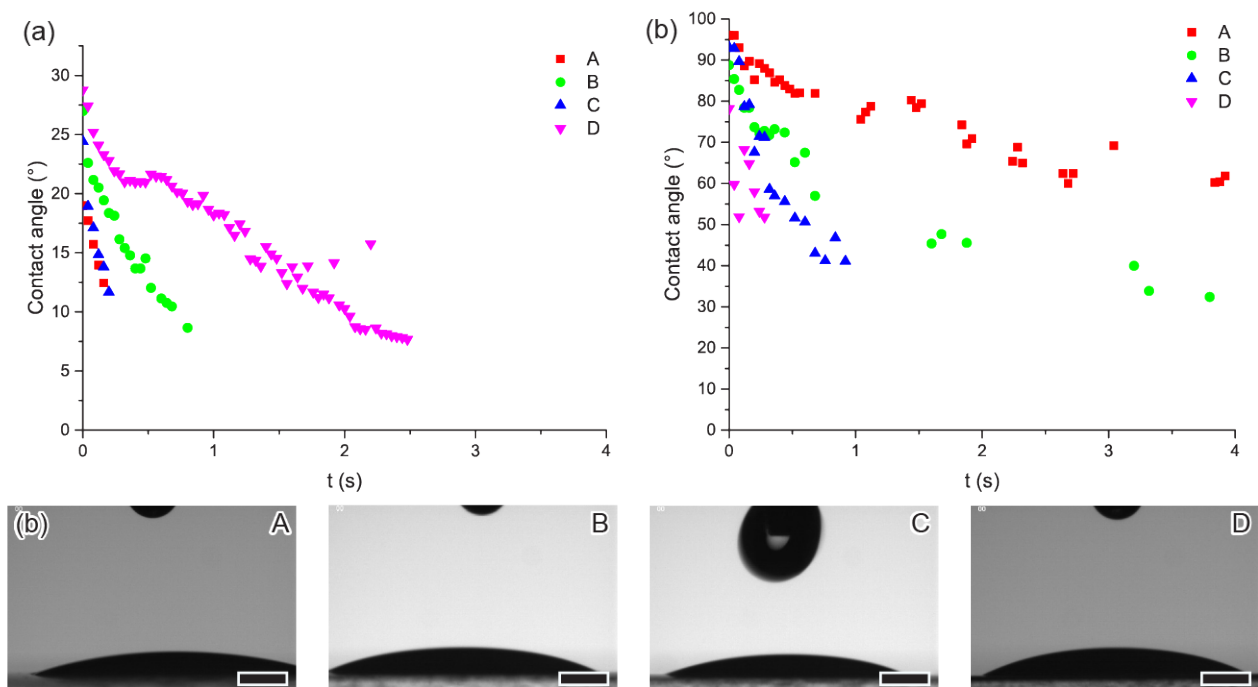
Figure 4.6: Contact angle over time for precursor dispersions A-D on PET substrate (a) in air (b) in water of pH 3, and (c) precursors droplets of compositions A-D in air at *t=0*. scale bar is 1mm.

from the interfacial tension between air and substrate being significantly higher than that of water and the substrate.

4.2.2 Altering continuous phase

As mentioned in section 4.2, precursor wetting could be improved by modification of the continuous phase. We have investigated two approaches. The first is to add 5 mM of CTAB to the continuous phase. We hypothesize that the hydrophobic tail of CTAB can adsorb on the substrate, which exposes the charged amine groups to the water phase. This makes the substrate more hydrophilic and thus lowers the substrate-water interfacial tension and the contact angle. The second method is the addition of ethanol to the continuous phase. This will lower the precursor-continuous phase interfacial tension, but it will also have an influence on ethanol diffusion. As the concentration gradient between inside and outside the precursor will be lower, the solvent diffusion will be slower, which will likely affects allow structures to coarsen more.

Figure 4.7 (a) shows the contact angles of precursors A-D in 5 mM of CTAB over time, as well as that of precursor A in water as a reference. The contact angles in CTAB for all four precursors are very similar. This implies that CTAB adsorbed to the substrate negates the difference between precursor compositions. The CTAB only decreases the contact angles for precursors A and B while they stay similar for C and D. Figure 4.7 (b) shows the contact angles of precursor A in water with 5, 10, and 20 v.% of ethanol over time. We expect that the addition of ethanol to the continuous phase would decrease the contact angle for all precursors as it decreases the polarity of the continuous phase. Precursor A is shown as this showed the biggest difference over the different ethanol contents. However, there is only a slight trend of the contact angle decreasing with increasing ethanol content. One would expect that the contact angle would decrease slower over time with higher ethanol concentration, as ethanol diffusion should slow down with a lower concentration gradient between inside and outside the droplet. This effect is not visible from these measurements. The addition of ethanol to the continuous phase is not useful to improve wetting, as the improvement is negligible, while it will likely influence the membrane structure. This could

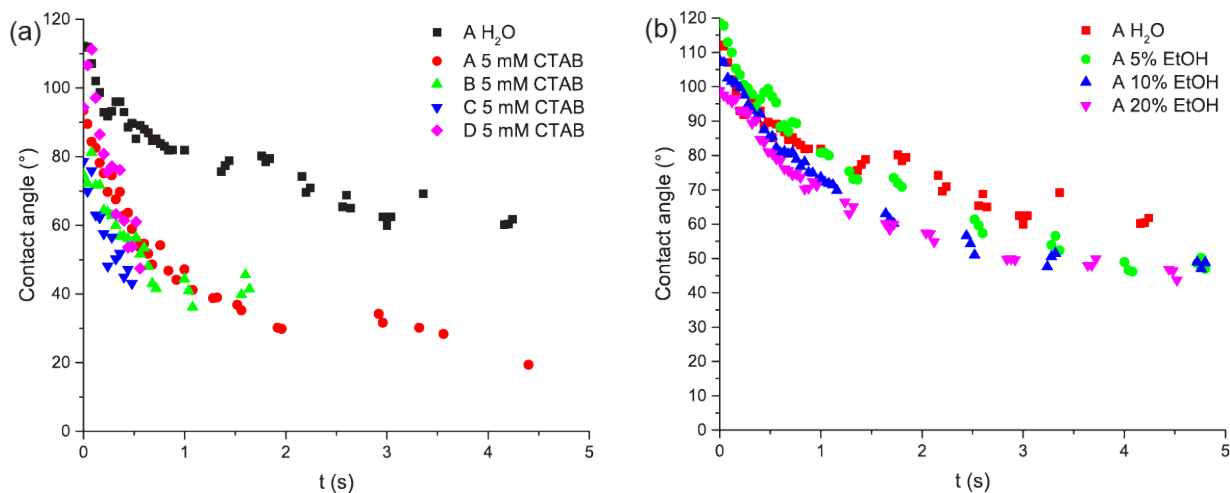mean that the precursor-continuous phase interfacial tension has less influence on the overall wetting.

Figure 4.7: Contact angle over time on PET substrate for (a) precursor dispersions A-D in water pH 3 with 5 mM CTAB, and precursor A in water pH 3 as a reference (b) precursor dispersion A in water at pH 3 and in with 5, 10, and 20 v.% ethanol.

4.3 Membrane structure

This section will show the dependence of membrane structure on the composition of precursor dispersion, and connect this to how the structure affect properties such as selectivity, throughput, and mechanical strength. As explained in section 2.2, to optimize the filtration properties of membranes, we want to control over properties such as pore size, pore size distribution, and connectivity of pores, as these determine factors such as selectivity and throughput.

We will discuss structures of membranes produced from precursor dispersion A-D with a range of CTAB concentrations and particle weight fractions displayed in Figure 4.8. The compositions have been chosen with oil contents higher than the critical point, so there is high BDA incorporation to form a mechanically stable membrane scaffold.

4.3.1 Internal membrane structure

The structures of STrIPS membranes can be divided into two groups, first in interconnected, spinodal structures, and second, droplet-dominated structures (Figure 4.9(a)). The interconnected structures can be further divided into three subgroups. There are the bi-continuous sponge-like structures that have pores connecting in a continuous network and have a high surface area[37](Figure 4.9(b)). Then there are the finger-like void structures which connect to the membrane surface via vertical channels (Figure 4.9(c)). Lastly, there are droplet-dominated areas within interconnected structures that are either the result of secondary phase separation or are the result of local inhomogeneities caused by STrIPS (Figure 4.9(d)). The following three sections will discuss how precursor composition, CTAB concentration, and nanoparticle weight fraction result in these structures.

4.3.1.1 Composition variation

To undergo spinodal decomposition, the composition of a precursor dispersion has to be close to the critical point in the ternary diagram where the binodal and spinodal meet (Figure 4.8). Compositions close to this point will directly move under the spinodal into the unstable
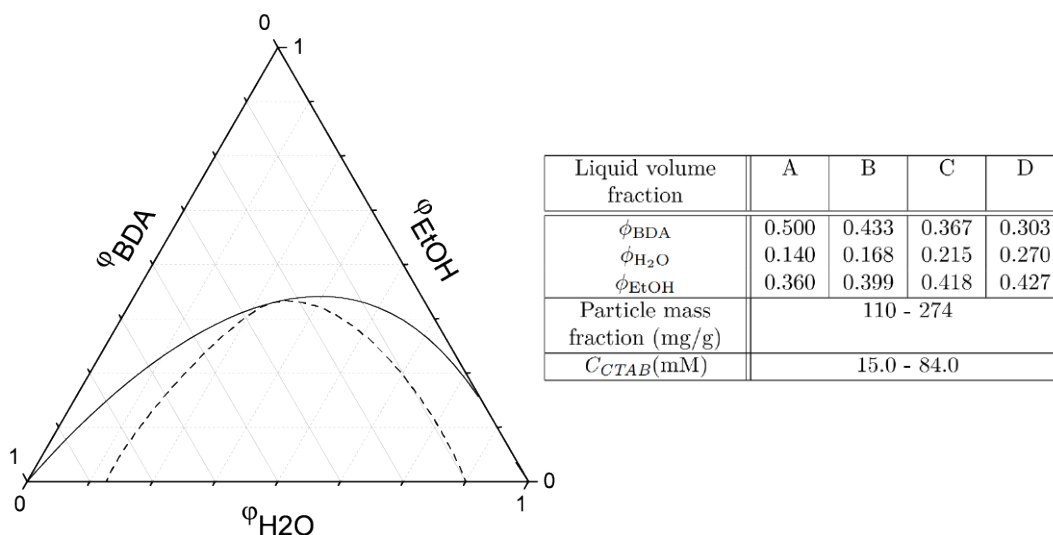
Figure 4.8: Ternary phase diagram for BDA/ethanol/water with precursor compositions labelled as A, B, C, and D. The area below the dashed line indicates the region of spinodal decomposition of the ternary liquid mixture. Liquid volume fractions are expressed by φ.

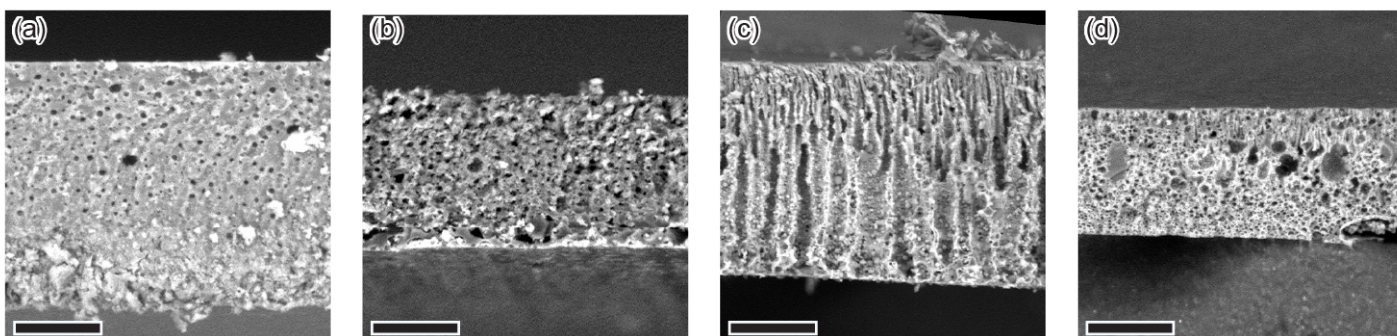| Liquid volume fraction	A	B	C	D
ϕ_{BDA}	0.500	0.433	0.367	0.303
ϕ_{H_2O}	0.140	0.168	0.215	0.270
ϕ_{EtOH}	0.360	0.399	0.418	0.427
Particle mass fraction (mg/g)	110 - 274			
C_{CTAB}(mM)	15.0 - 84.0			

Figure 4.9: SEM figures of cross-sections of (a) Fully droplet-dominated structure (b) Sponge-like structure (c) Finger-like void structure (d) Partly droplet-dominated membrane, with the top of the membrane shown on top. Scale bar is 20 µm.

region of the ternary phase diagram, where spinodal decomposition happens. Compositions further from this point will move to the area between the spinodal and binodal as ethanol diffuses out, where the composition is metastable which results in nucleation and growth.

The four compositions that have been used in this work, have higher BDA content than the critical point, so the expectation was that only those closer to the critical point would result in bicontinuous structures. Figure 4.10 (a) shows SEM images of the cross-sections of membranes made from precursor dispersions A-D with a CTAB concentration of 15 mM and with a particle weight fraction of 110 mg/g. The images show how, as expected, membranes made with compositions farther off the critical point A and B yield fully droplet-dominated structures, while membranes made with the compositions closer to the critical point C and D have more interconnected structures. This corresponds to the expectations.

Membranes A and B have been produced with CTAB concentrations of up to 70 mM to see if this could change the structure. This did however not yield significant structural change, as can be seen in Appendix A. Therefore, these compositions are disregarded in further structural analysis.

From the SEM images and 3D confocal reconstructions in Figure 4.10, one can see that for membranes made with compositions C and D, of which the structure result from spinodal decomposition, the pores at the surface are small, and undergo coarsening when going down
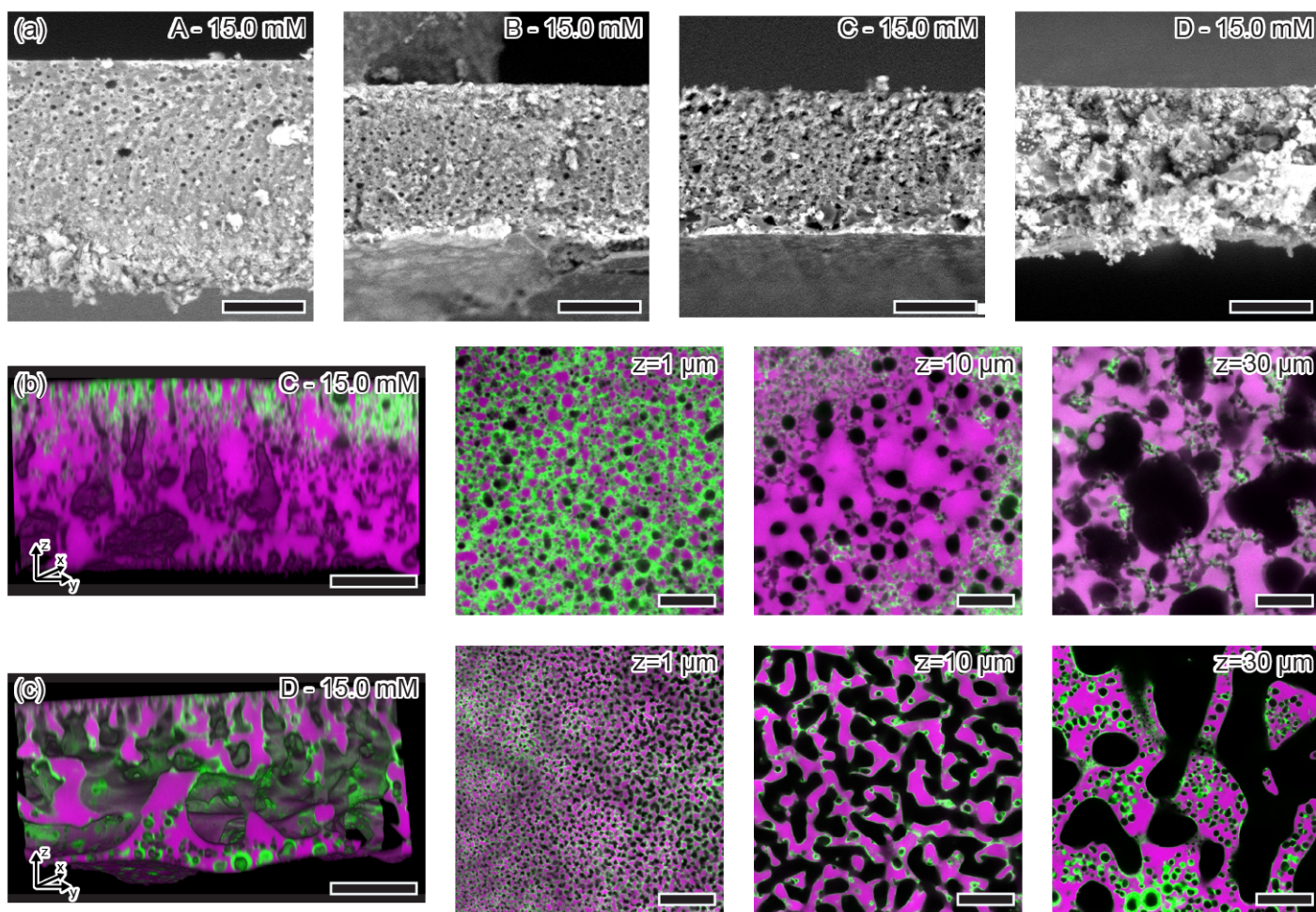
Figure 4.10: (a) SEM images of membranes made with precursor dispersions A-D with a CTAB concentration of 15 mM and a particle weight fraction of 110 mg/g. Side views of 3D reconstructions from confocal z-stacks of membranes made with composition C (b), and D (c) with 15 mM CTAB and 110 mg/g nanoparticles, together with confocal images taken at 1, 10, and 30 µm from the top surface. Particles are shown in green and oil is shown in magenta. Scale bar is 20 µm.

the z-axis. This is a trend which is inherent to STrIPS bijels[8]. This is because at high ethanol concentrations, the attachment energy of particles to the interface is lower, which delays arresting of the structure. Therefore, if ethanol diffusion is slow, there is more time for the structure to coarsen before it is arrested by the particles. As at the top of the membrane there is a high concentration gradient, the diffusion is fast and thus the pores are small. Deeper in the membrane, the gradient is less and the oil/water domains more coarse. The confocal images in Figure 4.10 (b) and (c) provide a better view of the structure of membranes C and D in the xy-plane. It shows how the structure of membrane D is spinodal like, how it coarsens over the z direction from domains in the micrometer size range at 1 µm depth to domains of about 10 µm in size at 30 µm depth, and how droplet-dominated domains form inside the oil phase though secondary phase separation. This is an indication that the particles must have a contact angle close 90°which allows the stabilization of this structure. The structure of membrane C is not completely bicontinuous, but the pores are still interconnected to some degree. In the image at 10 µm deep, it seems like there the structure is formed from a combination of water and oil droplets, where the droplets where the droplets of the same phase connect. This is potentially a permeable structure where liquids can flow across the membrane, and thus it is further investigated to see how the
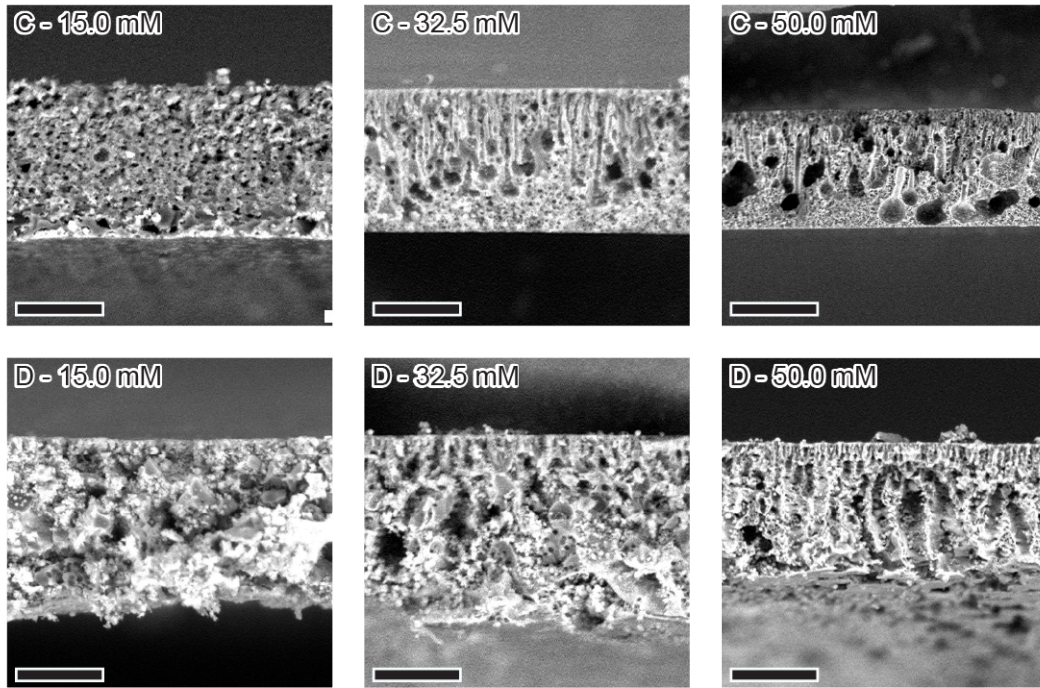
Figure 4.11: SEM images of membranes made with precursor C and D with a particle weight fraction of 110 mg/g and with CTAB concentrations of 15.0, 32.5, and 50 mM. Scale bar is 20 µm.

structure can be adapted.

4.3.1.2 CTAB concentration variation

We use CTAB to hydrophobize the silica nanoparticles by adsorbing to the negative charge of dissociated hydroxyl groups. This is done to make the particles neutrally wetting, which is preferred as it both increases the particle attachment energy, and allows for stabilization of irregularly shaped interface of a bijel. Variation of the CTAB concentration can therefore lead to a change in the preferred curvature, meaning that precursor dispersion composition which results in a droplet dominated structure at one CTAB concentration results in a spinodal structure at another concentration. As we have seen in Section 2.1.2.1, the particle attachment energy is dependent on the contact angle of the particles, and thus also on the CTAB concentration. As the particle attachment energy has an effect on the speed at which phase separation is arrested, and thus the amount of coarsening that is observed, this means that the CTAB concentration can have an effect on how much the membrane structure coarsens as well.

The effect of the CTAB concentration on the membrane structure of compositions C and D has been investigated by varying the concentration from 15 to 50 mM of CTAB with a constant nanoparticle weight fraction of 110 mg/g of precursor dispersion. Figure 4.11 shows these membranes at CTAB concentrations of 15.0, 32.5, 50.0 mM CTAB. At the lowest concentrations, the structures are more homogeneous over their depth, but the trend shifts to more vertically aligned structures with increasing CTAB concentration. The vertically aligned channels could be stabilized more at higher CTAB concentration, as the particles are more hydrophobic and thus stabilize a cylinder more than a spinodal structure. This trend is observed for both compositions, however, the structure of these vertical channels is contrasting.

Figure 4.12 shows 3D reconstructions from confocal z-stacks and confocal images of membranes C and D at 50 mM CTAB, confocal images at 32.5 mM CTAB can be found in

Appendix C. This shows how membrane C is droplet-dominated in structure, apart from the larger voids that connect with the surface through small and straight channels. It is possible that these channels form from droplets that have grown in size deeper into the membrane to the top surface of the membrane through some convective flow. This is not the case for the channels of membrane D, which are contrastingly continuously connected, and seem to have grown from the top to the bottom of the membrane. This likely difference in formation pathway is further discussed in section 4.4.
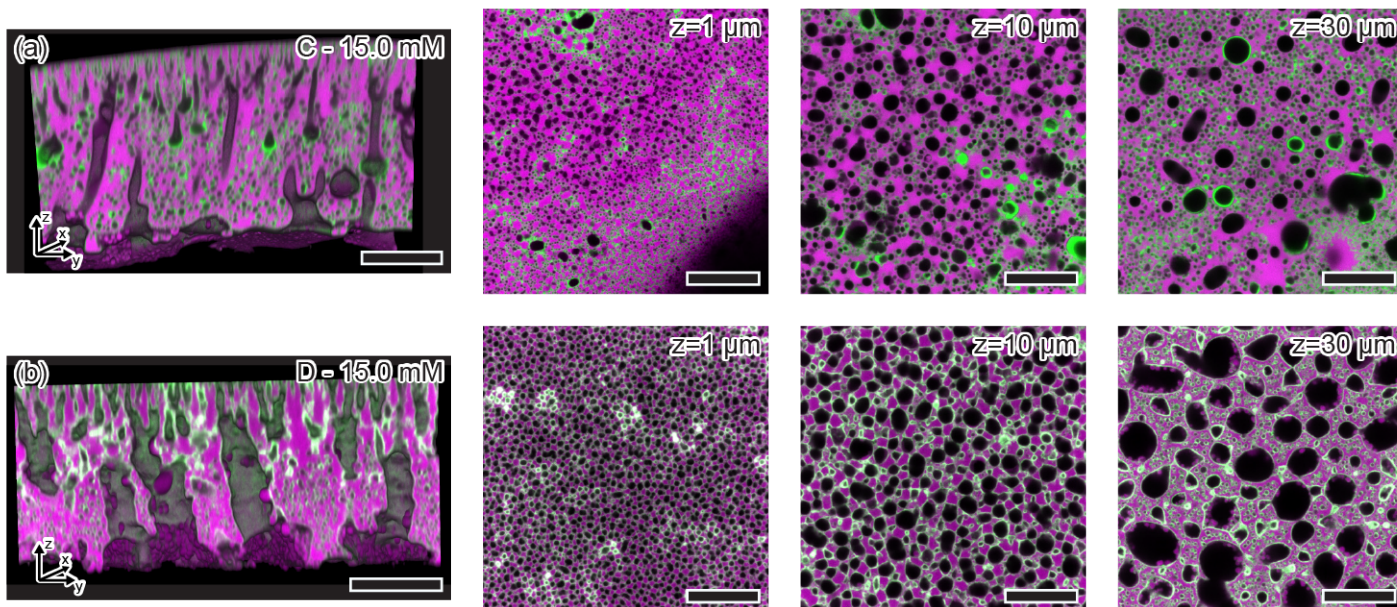

Figure 4.12: 3D reconstructions from confocal z-stacks of membranes made with precursor dispersion (a) C and (b) D at 50 mM of CTAB and 110 mg/g nanoparticles. With confocal images that are taken at a distance from the top of 1, 10, and 30 µm. Scale bars are 20 µm.

We have seen in Figure 4.10 that the phase separation for compositions A and B proceeds via nucleation and growth, while composition C and D decompose spinodally. However, in membranes with composition C we see that this spinodal decomposition result in a structure dominated by water-in-oil droplets. Furthermore, when looking at the confocal images in Figure 4.12, we can see that in the xy-plane the structure looks like droplets of water in the oil. We therefore hypothesize that at higher CTAB concentrations, the spinodal structure we observe for composition D at 15 mM can no longer be stabilized by the now more hydrophobic particles, and thus the structure is deformed into vertical channels that have a higher curvature towards the water phase. As composition C has a lower water content, maintaining a continuous water phase is comparetively harder, and thus the higher particle hydrophobicity results in a structure that deforms to completely droplet dominated.

4.3.1.3 Nanoparticle concentration variation

In order to investigate the effect of the nanoparticle concentration on the membrane structure, membranes with precursor dispersion composition D, a CTAB concentration of 50 mM, and particle weight fractions of 137, 210, and 272 mg/g of precursor dispersion have been produced. The precursor dispersions with 210 and 272 mg/g particle weight fraction did not produce membranes that are homogeneous over their width. Instead, the resulting membranes consist of several strips that show severe cracks after drying (Figure 4.13. The cracks are a result of shrinkage, which has been observed to a lesser degree in other membranes (section 4.1).
The shrinkage is likely caused by that the space in between nanoparticles is initially filled

with water, which evaporates during drying. This causes the particles to become packed more closely, and thus the membrane shrinks. Therefore, the high particle concentration membranes shrink, and thus crack, relatively more. The striped coating is likely caused by the increased viscosity of these precursor dispersions.
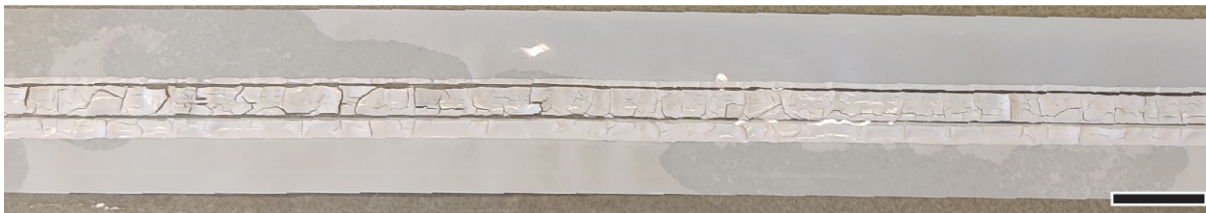

Figure 4.13: Membrane D with 84 mM CTAB, and 274 mg/g nanoparticle weight fraction. Scale bar is 20 mm.

The parts with most homogeneous height of these membranes were used for SEM imaging, of which the results can be seen in Figure 4.14. These parts are significantly thicker than the membranes with lower particle concentration as the precursor dispersion is not evenly spread, and the membranes are more inhomogeneous in thickness over their width. The figure reveals the trend that higher particle loadings lengthen the z-channels and decrease the gradient in the pore size over the depth of the membrane. Similar behaviour of vertical channels extending has been observed in polyelectrolyte hollow fibre membranes made using aqueous phase separation (APS)[38]. In that method, phase separation is induced by a buffer solution diffusing into the fibre instead of ethanol diffusing out. They conclude that the lengthening is caused by an increase in phase separation speed. This could be analogous where not the phase separation itself is faster, but it is arrested faster due to the high availability of particles. However, as structure formation in APS is more dependent on the change of viscosity than it is in STrIPS, the comparison is limited.
Another interesting observation is that while the channels are very straight, the confocal image at 60 µm from the top surface in Figure 4.14 (b) still shows that they are interconnected, this is likely due to the increase in pore size making the cylindrical pores overlap and thus connect. It is noteworthy in Figure 4.14 (c) that at the bottom of the SEM image, the membrane structure is less well-defined, which is a result from polymerization of precursor dispersion that has not finished phase separating. Other membranes that are also polymerized at 150 cm from the deposition nozzle, corresponding to 30 seconds of travel time, have completely phase separated. It seems that the ethanol diffusion in this high nanoparticle concentration membrane is slower.
The ethanol diffusion speed could be caused by the pore structure hindering diffusion. Data on the structural evolution of two membranes with different pore structures, which will be discussed in section 4.4, does however show that the difference in structure hardly influences the ethanol diffusion. It could therefore also be the case that the higher viscosity of higher concentration nanoparticle dispersions causes the slower diffusion. As ethanol diffuses out, the concentration of nanoparticles increases. In this membrane, which already has a high starting particle concentration, the effect on viscosity is more pronounced as the viscosity scales exponentially with particle volume fraction[39].
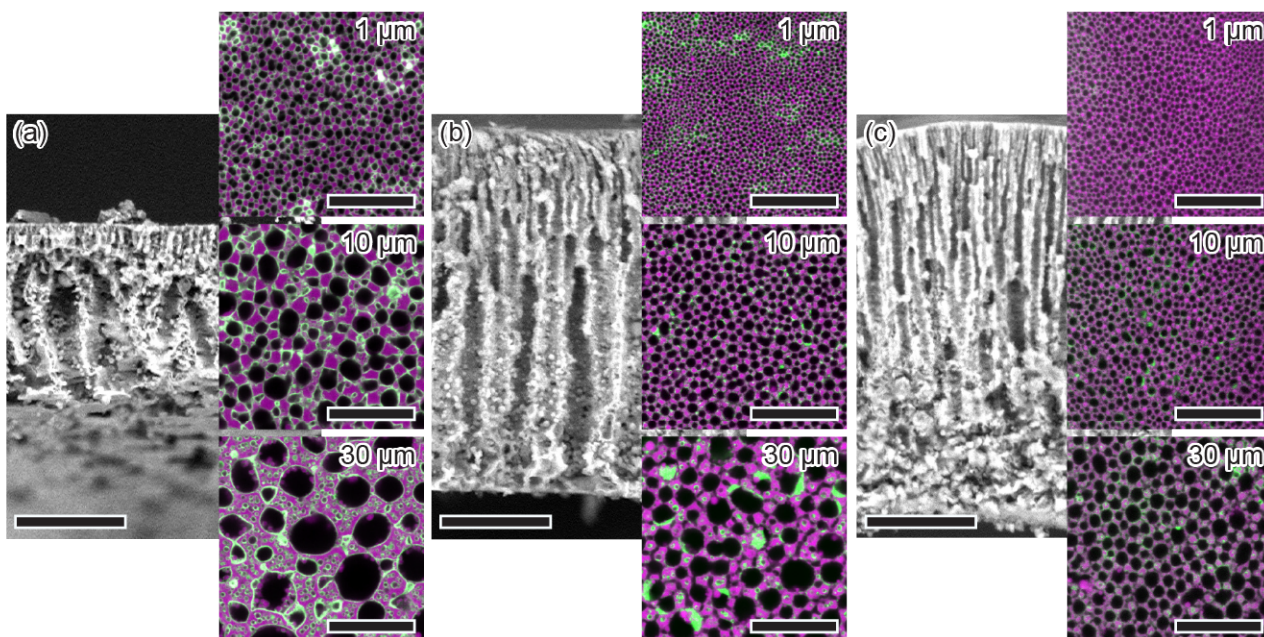
Figure 4.14: SEM images of membranes made with precursor dispersion D with 50 mM of CTAB and 137, 310, and 272 mg/g nanoparticles. With inlays of confocal images where BDA is displayed in magenta and particles in green, the images are taken at a distance from the top of 1, 10, and 30 µm. Scale bars are 20 µm.

4.3.1.4 Confocal analysis

Using Laser Scanning Confocal Microscopy, we can visualize the 3D structure of membranes by scanning through the volume, and measuring the emission of laser excited dyes that are in the oil and adsorbed to the particles. Confocal micrographs are taken in the x-y plane, and can be reconstructed into a 3D structure via extrapolation between micrographs taken at different z-coordinates. The confocal images also allow us to calculate the surface area of the membranes by determining the length of the oil-water interface of a single slice, and multiplying this with the thickness of a slice. The analysis of the confocal data can be used for a more numerical approach of describing and classifying the membrane structure.

Figure 4.15 shows the surface area and 3D reconstructions of three membranes that have a bicontinuous structure, a droplet-dominated structure, and a droplet-dominated structure with vertical channels. The profile of the surface area plots can be linked to the structure of their respective membranes. A bicontinuous membrane has fine pores at the surface, which coarsen over the depth, which results in a high surface area at the top which decreases quickly. The surface area curve flattens off deeper in the membrane where the structure coarsens slower, and the surface area of water droplets in the oil channels that form due to secondary phase separation increases. This is in contrast with the surface area of a droplet-dominated membrane, which is more constant throughout the complete depth, which is expected as its structure is more homogeneous. Last, the surface area of the droplet-dominated membrane with vertical channels is a mix between the other two structure, the surface area stays relatively similar throughout the membrane, but decreases in the middle, where the vertical channels become bigger and end in droplet, and then increases at the bottom where the structure is droplet-dominated again.

These surface area plots can in this way be rationally connected to the membrane structure, however, we can not yet definitively couple a surface area plot to a structure. The surface area can be used to further quantize the trend seen in the previous section, where we could see that the vertical channels extend further into the membrane and are more consistent in size with increasing nanoparticle concentration. As can be seen in Figure 4.16,
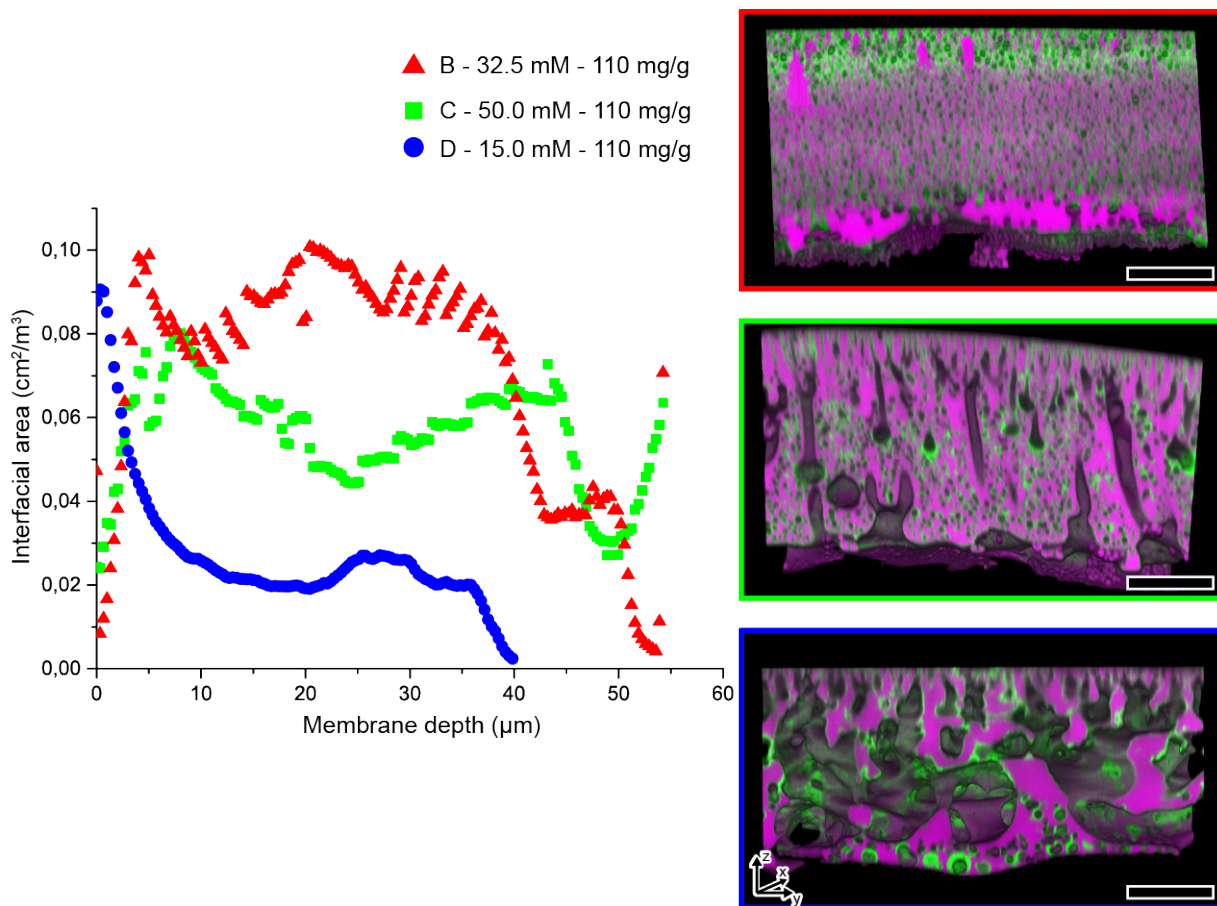
33

Figure 4.15: Interfacial area over membrane depth plot, and 3D reconstructions from confocal z-stacks of membranes B - 32.5 mM CTAB - 110 mg/g nanoparticles, C - 50.0 mM - 110 mg/g nanoparticles, and D - 15.0 mM - 110 mg/g nanoparticles. Scale bar is 20 µm.

this shows up in the surface area plots as a decrease in the slope.

While this shows that these plots can be indicative of trends, improvements in the measurements and more extensive analysis would be required to quantify the membrane structure. There are two problems with the confocal measurements that affect the results. First, the membranes are not exactly horizontal when the z-stacks are measured, this means that the upper micrograph of a z-stack is only partially measuring the actual membrane, which is the cause of a seemingly low surface area at the top of the membranes. An attempt was made to remedy this by measuring the z-stacks in between two microscopy slides to weigh down the membrane, but this did not eliminate this problem.
Second, the earlier discussed damage to the bottom surface of the membrane makes it hard to accurately determine what the surface looks like, this could possibly be remedied by doing the measurement while the membrane is still attached to the substrate, which could be possible as PET is does not absorb in the region between 488 and 700 nm which is used for excitation and detection[40].
Steps in improving the confocal data analysis can still be taken by differentiating between primary and secondary phase separation surface area. Furthermore, the bicontinuity of the structures could possibly be quantified with a measure of the curvature of the surface. This could differentiate between nucleated droplets that only curve in one direction, while the curvature of a bicontinuous structure can invert.
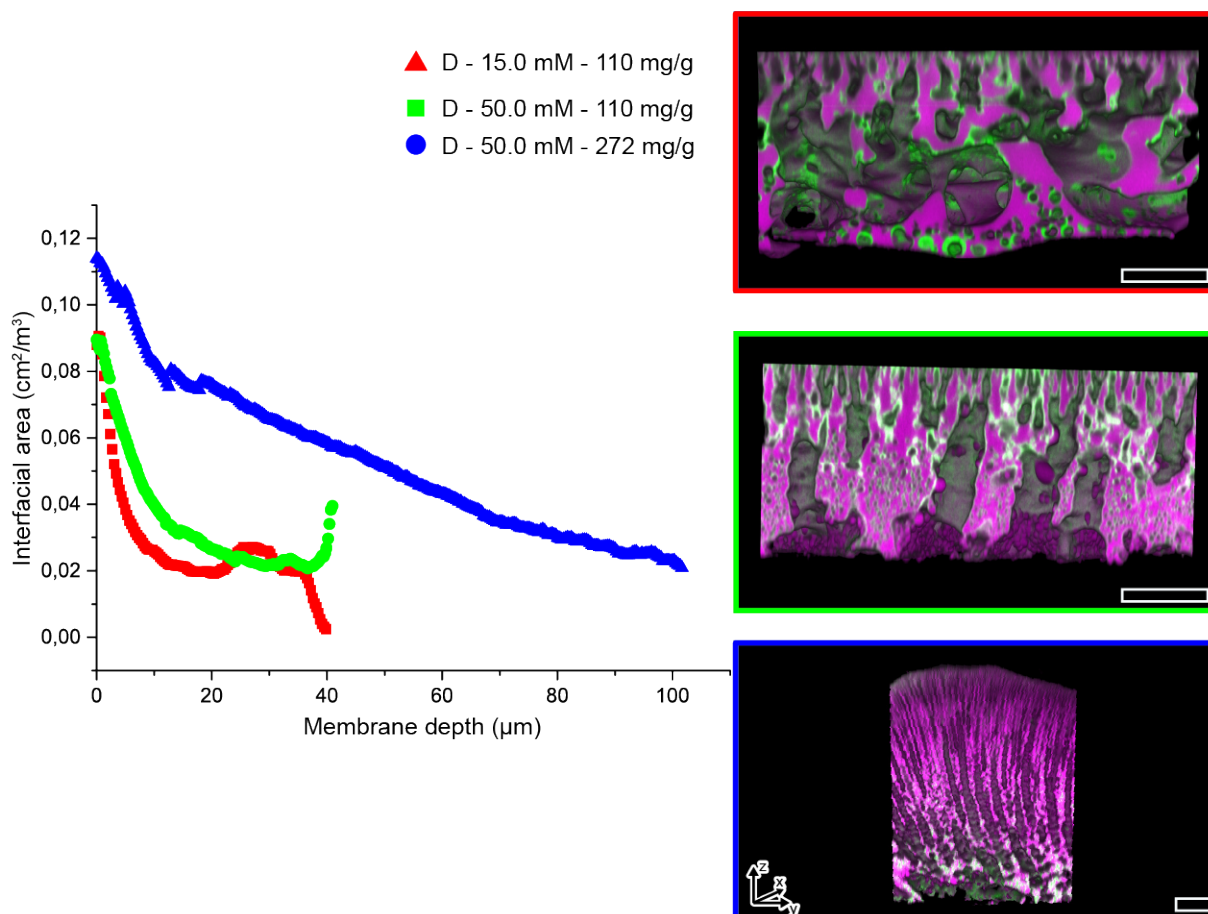
Figure 4.16: Interfacial area over membrane depth plot, and 3D reconstructions from confocal z-stacks of membranes D - 15.0 mM CTAB - 110 mg/g nanoparticles, D - 50.0 mM - 110 mg/g nanoparticles, and D - 50.0 mM - 272 mg/g nanoparticles. Scale bar is 20 µm.

4.3.2 Top surface

We hypothesize that the size of the surface pores can be controlled by increasing the particle weight fraction. At a higher particle concentration, there will be more clusters of particles that stick to the interface, which will narrow the resulting pores.

The average and standard deviations of the pore size of membranes C and D with a range of CTAB and nanoparticle concentrations are presented in Table 4.1. For precursor C there seems to be a trend of the pore size increasing with increasing CTAB concentration, however, this is not the case for precursor D, which stays more or less stable. Furthermore, there seems to be a slight decrease in pore size at a particle weight fraction of 137 mg/g, which stays stable with further increase.

The decrease in pore size with increasing particle concentration could be an indication that the hypothesis is true, and the increase in pore size could be due to the increase in CTAB decreasing the nanoparticle attachment energy, and thus allowing the pores to grow slightly larger. It is however more likely that these trends are perceived due to measurement error. The SEM images used to determine the top surface of the membrane do not have high contrast between the membrane surface and the pores, which makes accurate determination of the pore size difficult (Figure 4.17. This is caused by difficulties with getting the flat top surface into focus. To be able to make more definitive statements on the pore sizes, further efforts should be made to attain higher contrast images of the surface through means of sputter coating or higher resolution SEM.

Aside from being unable to definitively state these trends, we can conclude that the pores are at the micrometer length scale, which should corresponds to microfiltration separation

properties, but this needs to be verified- experimentally. Furthermore, it is not possible to change the pore size by an order of magnitude by varying the CTAB or particle concentration, which would be necessary to attain ultrafiltration properties. Work has been done to improve the selectivity of hollow fibres of the same BDA:water:EtOH system by deposition of polyelectrolyte layers on the surface, which should be transferable to these planar membranes[11].

Table 4.1: Pore sizes with standard deviation (StDev) for membranes produced using precursors C and D, with CTAB concentrations ranging from 15-50 mM, and particle weight fractions of 110 - 272 mg/g.

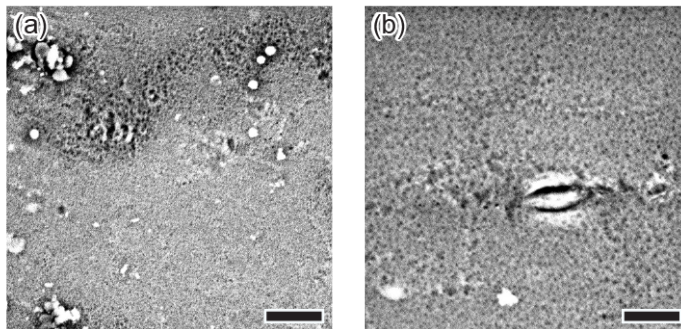| C_{CTAB} (mM)	Particle weight fraction (mg/g)	Pore size ±StDev (µm)	
		Precursor C	Precursor D
15	110	1.17 ±0.36	1.07 ±0.23
32.5		1.32 ±0.33	1.22 ±0.36
50		1.69 ±0.32	0.86 ±0.15
	137	-	0.81 ±0.09
	210	-	0.80 ±0.21
	272	-	0.96 ±0.18

Figure 4.17: SEM images of the top surface of membranes D - 50 mM CTAB - 210 mg/g nanoparticle weight fraction and D - 32.5 mM CTAB- 110 mg/g nanoparticle weight fraction. Scale bar is 10 230 µm.

4.3.3 Bottom surface

The bottom surface of a membrane should have pores connecting the interior to the outside and should not restrict throughput. This can be hindered by the formation of a thin layer of BDA on the hydrophobic PET substrate. Therefore, the porosity of the bottom surface is investigated using SEM imaging.
A problem in this investigation is that the bottom surface is easily damaged during removal of the dried membrane from the substrate. Figure 4.18 shows poly-BDA residue left on the substrate after removal, as well as SEM images of the damage caused to membranes.

As the damage is caused by mechanical stress during removal from the substrate, we hypothesized that it could be prevented by dissolving the substrate, since this would circumvent the application of mechanical force.
The substrate was dissolved by submerging pieces of membrane that were still attached to the substrate in Trifluoroacetic acid (TCA), Dichloromethane (DCM), and Tertrahydrofuran (THF). The PET substrate only dissolves completely in TCA, while DCM and THF caused the substrate to swell and deform (Figure 4.19 (a)). The membrane in TCA could be taken out without any substrate attached, while there still was substrate attached to the
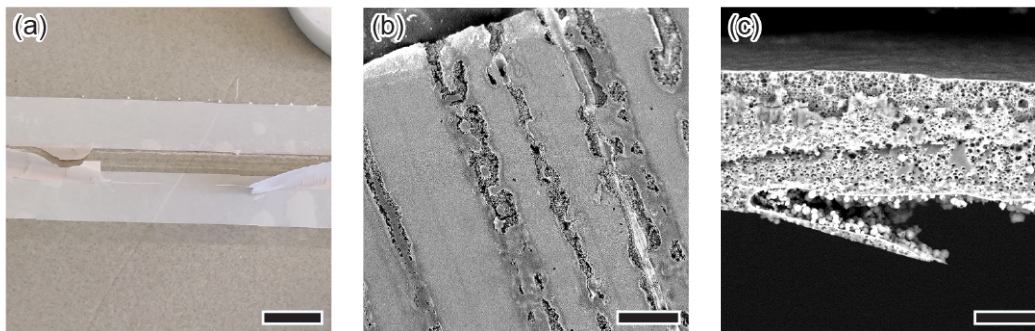
Figure 4.18: (a) Photograph of membrane sticking to the substrate. Scale bar is 20 mm (b) SEM image of damage caused by removal from substrate at the bottom of a membrane. Scale bar is 200 µm (c) SEM cross-section of damaged membrane caused by removal from the substrate. Scale bar is 20 µm.

membranes removed from THF and DCM. Figure 4.19 (b) shows residue left on the substrate after the membrane submerged in THF was separated from it, this shows that there is still damage done to the membrane. Similar results were observed for the membrane in DCM.
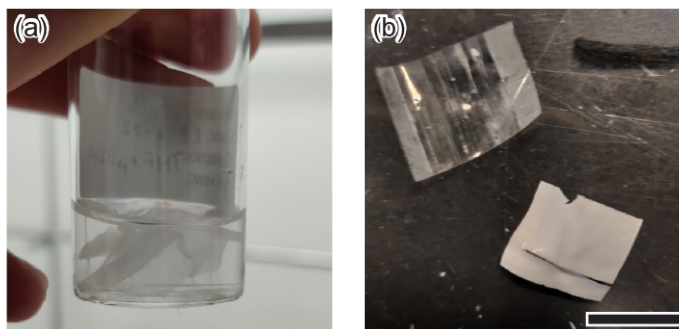

Figure 4.19: (a) Membrane submerged in THF (b) Membrane and PET substrate after being submerged in THF and separated. Scale bar is 10 mm.

Figure 4.20 shows a comparison of the bottom of membranes made with precursor D, 50 mM CTAB, and 110 mg/g nanoparticles. The membranes in (a) and (b) were removed from the substrate mechanically, while that in (c) was dissolved. On the membranes in (a) and (b) flakes of poly-BDA can be seen breaking off. Around the edges of where the bottom surface has broken off in (a) and (b), a similar structure is seen as in the undamaged membrane of which the substrate was dissolved in (c). It is thus likely that (a) and (b) had a similar structure on the bottom surface before the bottom was ripped off during substrate removal.

Further investigation shows that the bottom surface of the membrane that had the substrate dissolved is not completely homogeneous, which it does seem to be in Figure 4.20 (c). There are three types of surfaces that can be found on the bottom. The first type of surface is shown in Figure 4.21 (a), and is slightly inset from the substrate. It seems to be caused by a water-rich droplet forming on the substrate. The droplet surface is covered with nanoparticles, which makes it less porous. The second type of surface shown in Figure 4.21 (b) consists of a porous layer of oil with 1-3 µm pores that is dotted with larger 8-10 µm pores that provide connection to deeper in the membrane. The last type in Figure 4.21 (c) is a direct connection to the inside of the membrane, this is very similar to the damaged areas observed in other membranes. This could be an indication of either there still being damage even when the substrate is dissolved, or this structure is caused by inhomogeneous wetting and thus inherent to the membranes.
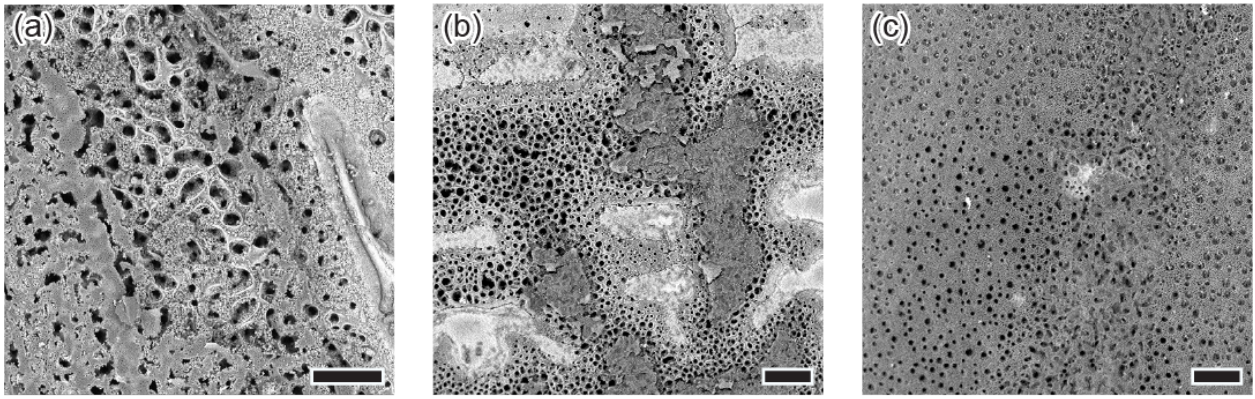
Figure 4.20: SEM images of membrane D - 50 mM - 100 mg/g (a-b) mechanically removed from the substrate, and (c) substrate dissolved in TCA. Scale bar is 100 µm.
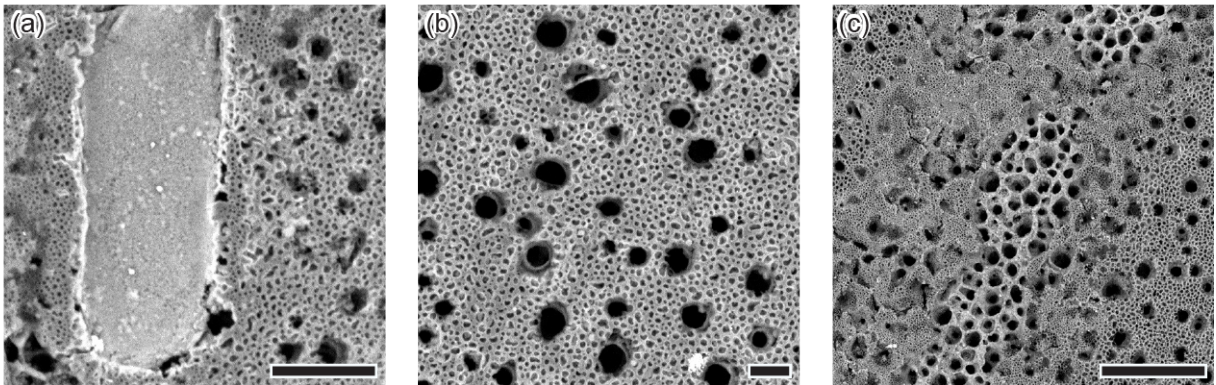

Figure 4.21: SEM images of the bottom surface of membrane D - 50 mM - 110 mg/g. Scale bar is 30 µm.

Most of the investigated bottom surface has the structure of 4.21 (b). We hypothesize that it forms due to formation of a thin layer of BDA on the substrate to which the small pores are introduced through nucleation of water droplets, while the larger pores form from the connection of internal channels to the bottom surface. If this is the case, we would expect that similar bottom structures should be found on membranes made with different precursors. Figure 4.22 shows the bottom surface of three membranes with (a) composition D, 15 mM CTAB, and 110 mg/g nanoparticles (Figure 4.12 (b)), (b) composition C, mM CTAB, and 110 mg/g nanoparticles (Figure 4.12 (a)), and (c) composition D, 74 mM CTAB, and 274 mg/g nanoparticles. These membranes did not have their substrate dissolved, and thus appear damaged. The internal structure at the bottom of the membranes are porous with large domains, nucleated, and vertical channel dominated for (a)-(c) respectively. All of these membranes do seem to have similar structured bottoms with a layer of BDA with small pores, and larger pores connecting to the internal structure, but the ratio between the two is dependent on how well internal pores connect to the bottom.

Ideally, the bottom surface would be completely homogeneous, and the areas from 4.21 (a) eliminated, as these areas are more restrictive towards flow due to their small pore size. This could possibly be achieved by using a porous substrate. This would allow ethanol to diffuse out, and thus phase separation to start, from both sides of the membrane. Phase separation from both sides would likely result in a more homogeneous structure, as the structure generally becomes more nucleated and harder to control deeper into a membrane. It is
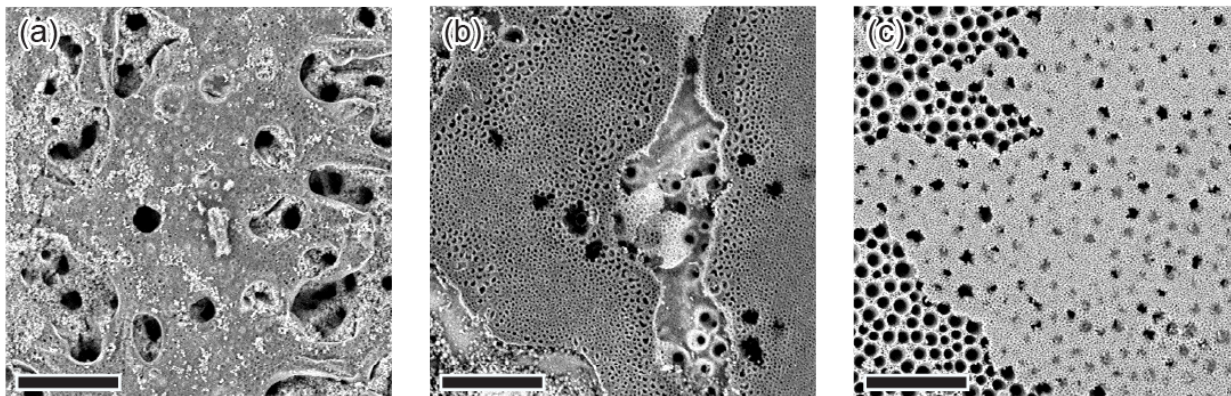
Figure 4.22: SEM images of the bottom surface of membranes (a) D - 15 mM CTAB - 110 mg/g nanoparticles, (b) c - 50 mM CTAB - 110 mg/g nanoparticles, and (c) D - 74 mM CTAB - 274 mg/g nanoparticles. Scale bar is 50 µm.

however also possible that the pores from both sides do not connect, so further investigation is required.

Another possible benefit of a porous substrate is that water channels can connect to the substrate pores. If the pores connect, the membrane would not have to be removed from the substrate, which allows the substrate to act as a support for the membrane. Both a more homogeneous structure and a porous support substrate will likely lead to a more mechanically resistant membrane, which will make allow higher pressures and thus higher throughputs.

4.4 Structural evolution

In the previous sections, we have studied the structures of STrIPS membranes, but we still lack insight in the formation mechanism of the membranes. We have investigated this process by polymerizing the membranes as phase separation is progressing, and by correlating this data with COMSOL Multiphysics solvent diffusion simulations. This experiment can be used to show if there is indeed a difference in the direction of growth of the channels in membranes C and D with 50 mM CTAB which was hypothesized in 4.3.1.2. However, this would require further experimental work, as the structural evolution of membrane C has not yet been investigated.

4.4.1 Variation of polymerization distance

We visualize the structural formation by polymerizing the membrane at different distances from the precursor deposition nozzle to the UV-lamp. Figure 4.23 shows how this distance is varied, and the resulting travel time from nozzle to polymerization. This travel time, or Δt, is the duration of time that solvent diffusion can take place.

Precursor dispersion D has been investigated at CTAB concentrations of 15 and 50 mM, as these result in a sponge-like and z-channel dominated structures respectively. Comparison of these different structures could give insight on the difference in their formation and the influence of structure on solvent diffusion.

Figure 4.24 shows the membranes polymerized at five of the nine recorded Δt, the full overview can be seen in Appendix B, and the phase separation front is marked in magenta. The phase separation front is plotted as depth in Figure 4.25. The images and plot show how in the first 600 ms the phase separation progresses quickly to about 10 µm deep, and how this speed drops off and follows a linear trend afterwards. It is noteworthy that up to 2.5 seconds after deposition, the phase separation front for both membranes has progressed

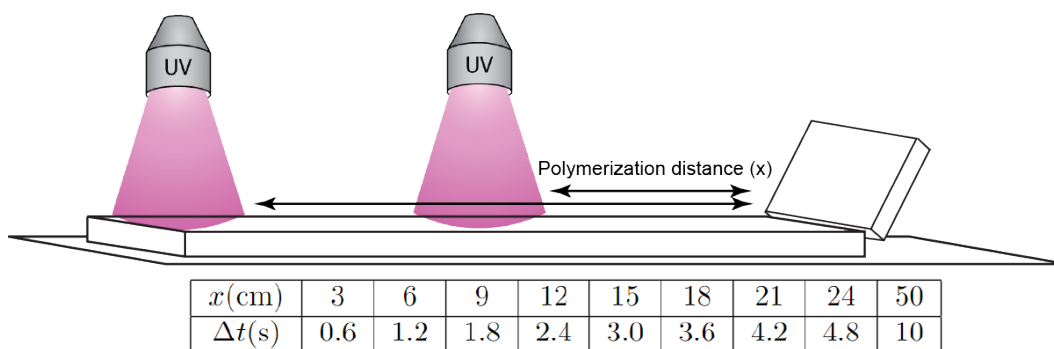| x(cm)	3	6	9	12	15	18	21	24	50
Δt(s)	0.6	1.2	1.8	2.4	3.0	3.6	4.2	4.8	10

Figure 4.23: Schematic of the variation of the distance between nozzle and UV-lamp. The table shows the polymerization distance and corresponding travel times.

at the same speed. This is unexpected, as this would mean that the internal structure has limited to no effect on the diffusion speed out of the forming membrane. This while the observation was made in section 4.3.1.2 that the pores of membrane D - 15 mM have less vertical channels, which could lead to a longer diffusion path length and thus slow down diffusion.

An interesting observation was made in the SEM images that show the structural evolution of film D - 15 mM. If we include time steps $\Delta t = 3600\ ms$, and $\Delta t = 4800\ ms$ in Figure 4.26, we can see cavities in the membranes. These can however not be found in membranes that have finished phase separating completely. This could either be due to structural evolution filling these cavities as time goes on, or by it being an inhomogeneity that is not often formed, and thus has not been detected in fully phase separated membranes. If it is caused by structural evolution, this would imply that at lower CTAB concentrations, the particles have a lower attachment energy deeper in the membrane and thus do not stabilize the BDA into a rigid structure. Instead, the BDA flows to the top of the membrane and there fills the observed cavities. This is contrary to what has been observed in membrane D - 50 mM, as the z-channels seem to form into their final structure immediately, and do not undergo change as STrIPS progresses at any depth.
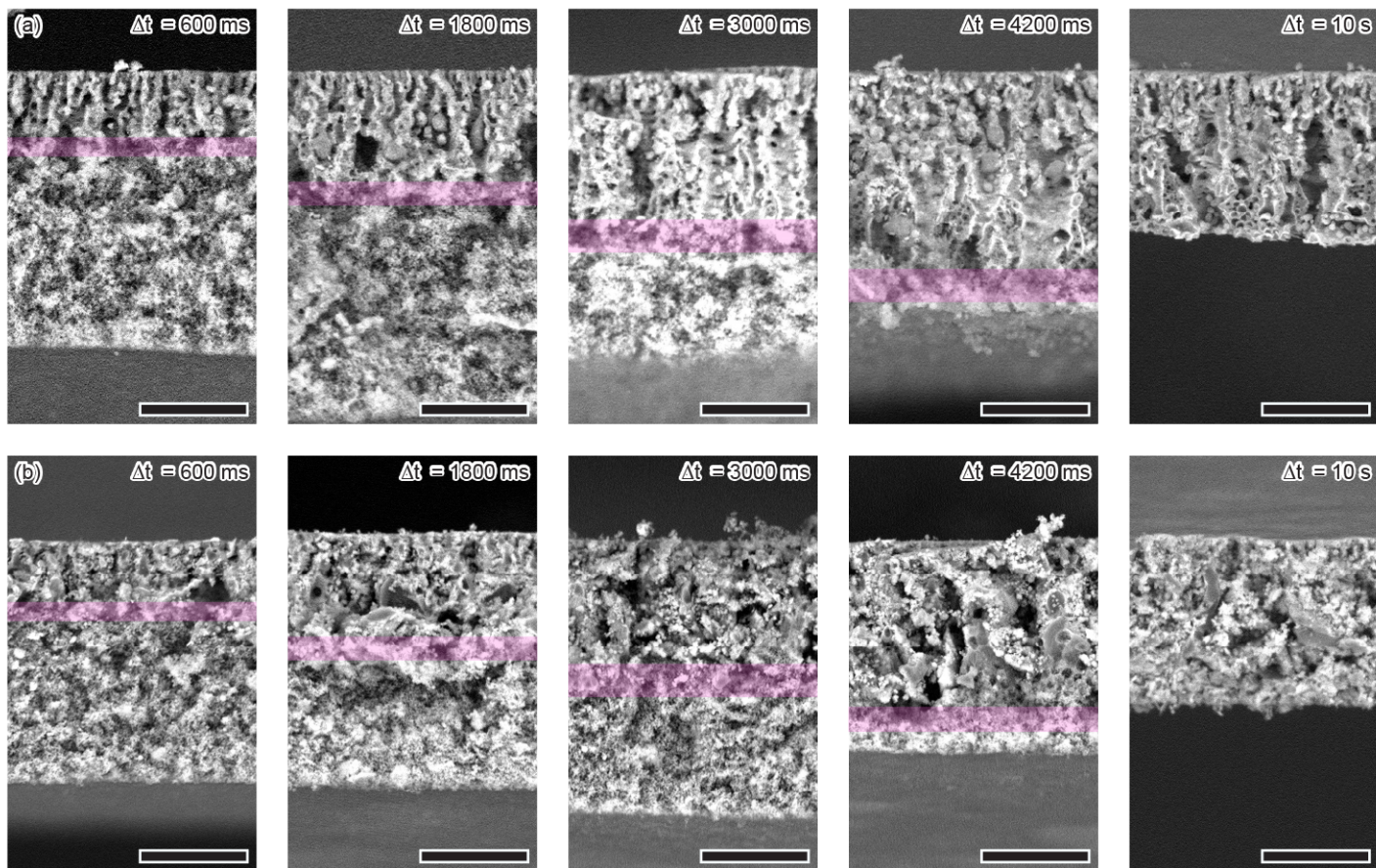
Figure 4.24: SEM images of membranes polymerized at travel times (Δt) from deposition nozzle to UV-lamp. Membranes are made with precursor D with a particle weight fraction of 110 mg/g and with CTAB concentrations (a) 50 mM, and (b) 15 mM. The front of phase separation is marked in magenta. Scale bar is 20 µm.
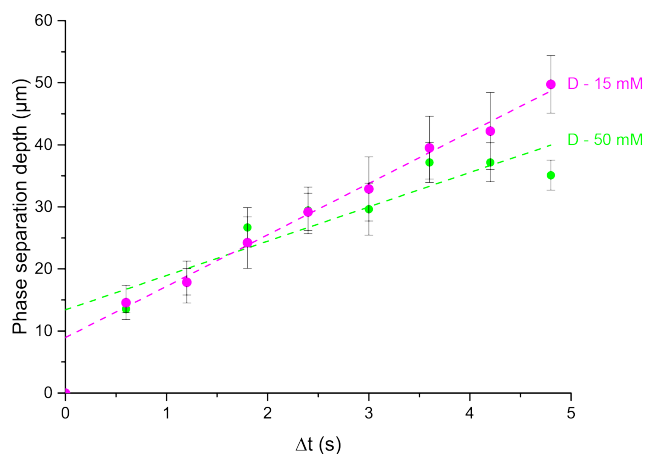

Figure 4.25: The polymerization depth over time is plotted for membranes D - 15 and 50 mM CTAB. The dotted lines indicate the linear fit of the data points.**Add the fit paramters**
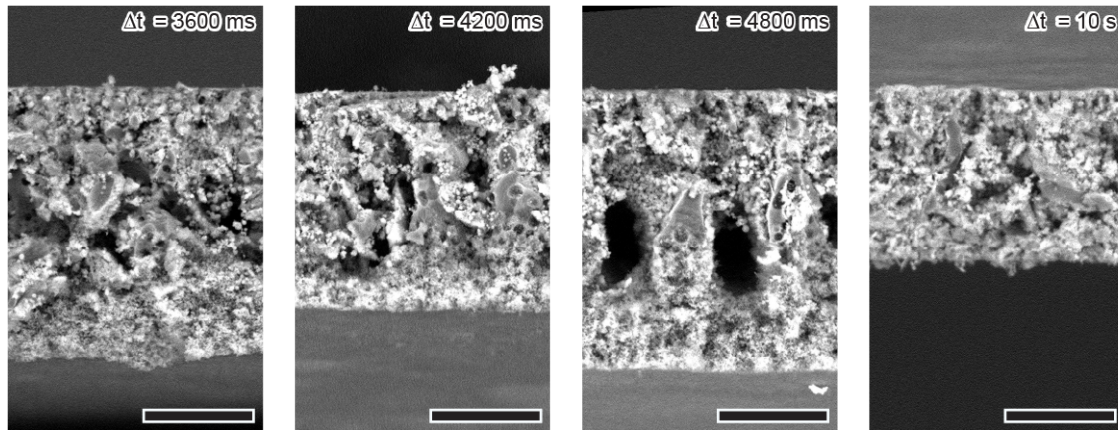
Figure 4.26: SEM images of membranes polymerized at travel times (Δt) from deposition nozzle to UV-lamp. Membranes are made with precursor D with a particle weight fraction of 110 mg/g and with CTAB concentrations of 15.0 mM. Scale bar is 20 µm.

4.4.2 COMSOL simulation

Diffusion simulations were performed to correlate with the experimental results. Previous work has shown that COMSOL simulations can approximate how the density changes and how phase separation progresses through a bijel fibre[41, 11]. The simulations of Siegel et al. showed that a small decrease in the ethanol concentration is enough to initiates phase separation, which is stems from the precursor compositions being chosen slightly above the binodal line and thus only a small ethanol fluctuation should initiate phase separation.

It is expected that the formation of the top surface with small pores hinders ethanol diffusion, which is modelled in this simulation by the formation of a diffusion barrier that starts at the top surface to 10 µm into the film, where the diffusion coefficient is lowered. This is the cause of the kink in the concentration profiles shown in Figure 4.27. This figure shows the simulated ethanol concentration profiles overlaid over the SEM micrographs of membranes polymerized at different Δt. This figure clearly shows that this solvent diffusion simulation does not correlate well to the experiments, as the ethanol concentration decreases faster than phase separation progresses.
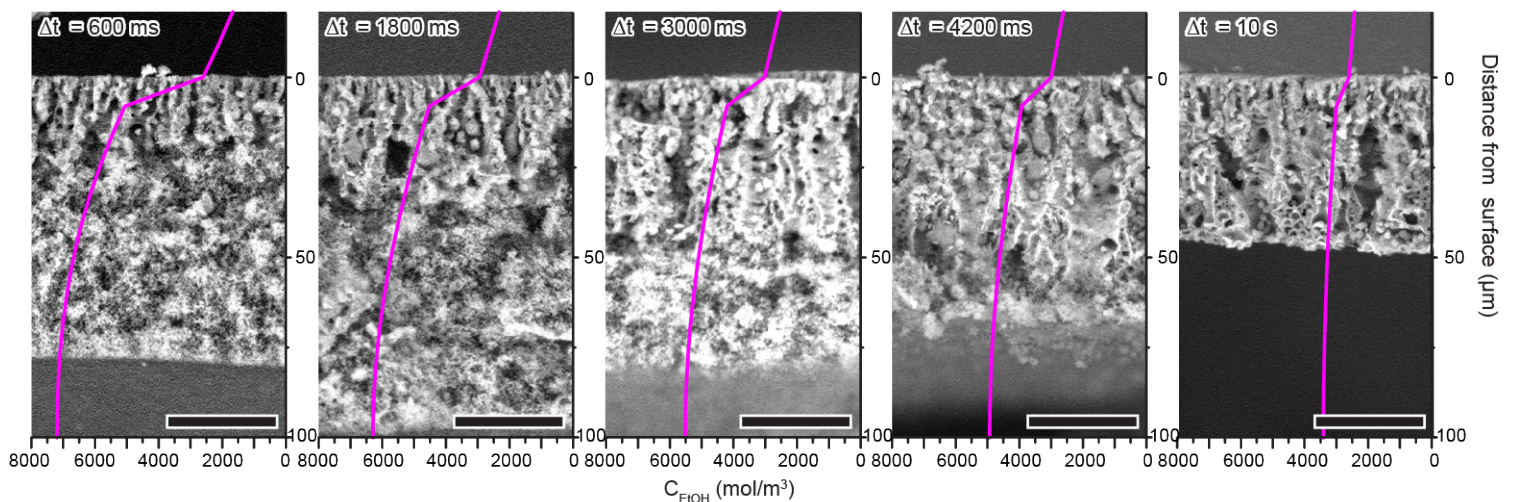

Figure 4.27: SEM images of membranes polymerized at different Δt, with the ethanol concentration profile overlaid.

This seems to be the case because the phase separation process takes about 5 seconds to progress to 60 µm deep compared to the fibres in the work of Siegel et al., which only take about a second to phase separate for a fibre with a radius of 60 µm. This difference can partly be explained by that the surface to volume ratio of a planar sheet is half that of a cylinder with the same radius as the thickness of the sheet. This means that double the volume of ethanol has to diffuse through the surface. The surface likely limits the outgoing ethanol diffusion to a specific volumetric flow, but the diffusion barrier in the model only decreases the diffusion constant at the top 10 µm of the film. This would however still not explain the complete difference between a planar and cylinder so other explanations should be found.

It is likely that the difference between simulation and experiments comes from oversimplification of the complex STrIPS process in the simulation, as the simulation assumes that diffusion happens homogeneously though the volume with the diffusion coefficient of ethanol in water. This ignores differences in diffusion between ethanol in oil or water, the creation of tortuous paths which lengthens the diffusion pathway, the interference of particles at the interfaces, changes in viscosity, and possibly more factors that we do not understand yet. Therefore, further work on expanding the simulations could be useful in explaining the difference between fibre and planar geometries.

A last noteworthy observation is that the ethanol concentration does not reach zero after 10 seconds even in this simulation, where the ethanol diffuses faster than in the experiments. This makes it likely that there is ethanol left in the membrane as it is polymerized.

4.5 Membrane thickness

The thickness of a polymerized membrane is a function of the thickness of the deposited precursor dispersion film on a substrate and the change of that thickness during STrIPS due to ethanol and water diffusion out of and into the membrane, respectively (Figure 4.28). The thickness of the deposited film (x) can be calculated from the volumetric flow rate Q, nozzle width W, and substrate speed u using equation 4.1. The thickness of the resulting membrane X can be calculated by multiplying with a prefactor ξ, that represents the change in thickness of the deposited film between deposition and polymerization, caused by ethanol diffusing outward (Formula 4.2).

$$x = \frac{Q}{Wu} \tag{4.1}$$

$$X = \xi \frac{Q}{Wu} = x\xi \tag{4.2}$$

The value of ξ is in between 1 and the combined volume fraction of water and BDA ($\phi_{H2O,BDA}$) in the precursor. It is however hard to accurately predict this value, as we know from simulations in section 4.4.2 that the ethanol concentration can be non-zero at the time of polymerization, and we have no data on the inflow of water. We can instead calculate ξ from experimental data.

Table 4.2 shows the thickness of the deposited precursor film, the average resulting membrane thickness, the minimum and maximum thickness measured, the calculated value for ξ, $\phi_{H2O,BDA}$, and the difference between ξ, $\phi_{H2O,BDA}$, for membranes made with precursors A-D. The data shows that the thickness of membranes A and B corresponds closely to that of $\phi_{H2O,BDA}$, membranes made with precursor C and D, are both thicker than expected from $\phi_{H2O,BDA}$. This can be explained by the structural differences between the membranes discussed in section 4.3.1.1. The structure of membranes A and B is completely nucleated, which does not allow for water to flow into them. This is different for membranes C and D as these have porous structures that potentially do allow that flow.

The thicknesses of the membranes shown in Table 4.2 are an average of 5-7 membranes made with CTAB concentrations between 15 and 75 mM of CTAB. . We hypothesize that the CTAB concentration does have an influence on the thickness, but there are several factors which introduce the large difference between the minimum and maximum measured
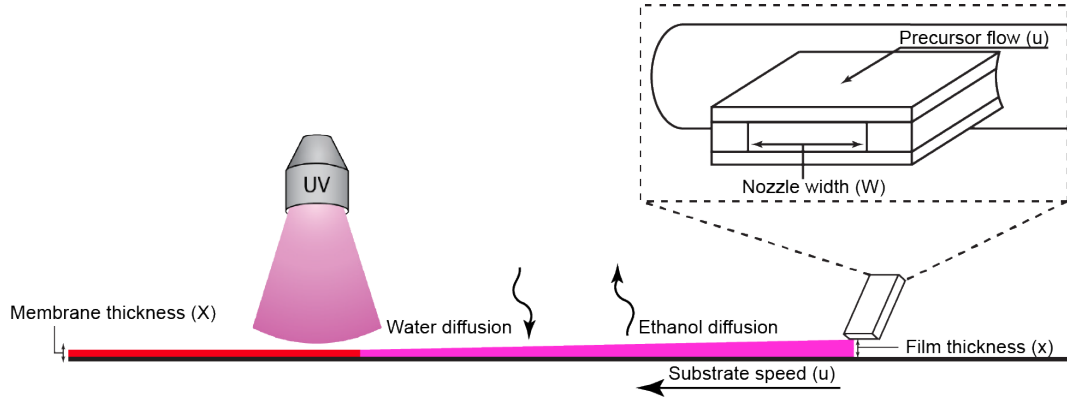
Figure 4.28: Schematic of the deposition of a precursor film with thickness x that is deposited with volumetric flow rate Q, that undergoes solvent transfer, and is polymerized into a membrane of thickness X. The width of the nozzle is indicated by W, and substrate speed by u.

Table 4.2: Thicknesses of membranes produced with precursor dispersion A-D, together with the thickness of the thickness of the deposited film (x), the change in thickness between the deposited film and the resulting membrane expressed as ξ, the volume fraction of BDA+water in the precursor $\xi - \phi_{H2O,BDA}$, and the difference between the two.

		A	B	C	D
Membrane thickness X (µm)	average	45.5	42.2	47.1	46.8
	minimum	26.3	28.1	34.3	25.1
	maximum	70.5	57.2	69.9	72.3
Film thickness x (µm)		71.7			
ξ		0.634	0.589	0.656	0.653
$\phi_{H2O,BDA}$		0.640	0.601	0.582	0.573
$\xi - \phi_{H2O,BDA}$		-0.006	-0.012	0.074	0.080

thickness in the data. This inaccuracy allows us to only say that the precursor composition, does have an influence on the membrane thickness, but further investigation is needed for exact determination of ξ, and the effect of CTAB on it.

The three main factors that cause the large difference are the damage to the bottom of the membranes, variation in thickness over the length of the membrane, and a difference in width between the three used nozzles. When measuring the thickness, damaged areas are not measured, which results in falsely measuring a lower thickness. The variation over the length of the membrane is caused by instabilities in the coating machine. Attempts to increase the stability of the substrate and nozzle during coating have decreased the variation, but have not eliminated it. The last problem causing the variation in thickness is that for this data set, three nozzle with widths of 8.5, 9, and 10 mm in width have been used. This was noticed after the production of the membranes, and therefore the variation in precursor film thickness that this introduces could not be taking into account during data analysis.

Conclusion and outlook

In this work, we have shown that we can reproducibly make bijel templated membranes in a continuous roll-to-roll process via solvent transfer induced phase separation (STrIPS), and that we have control over the membrane structure.

The membranes are produced by coating of a precursor dispersion consisting of butanediol diacrylate (BDA), ethanol, water, and CTAB functionalized Ludux TMA nanoparticles on a polyethylene tetraphtlate (PET) substrate, and subsequent photopolymerisation of BDA. This results in solid membranes with highly interconnected pores, of which the structure is fine at the surface and coarsens further from the surface, and which has a surface pore size in the micrometer range. We have found that precursor compositions further from the critical point phase separate through a nucleation and growth process, while those closer to the critical point decompose spinodally. Mixtures that undergo spinodal decomposition can however still result droplet-dominated structures or structures with cylindrical pores when high CTAB concentrations are used, as the particles are then more hydrophobic and thus preferentially stabilize an interface curved towards the water phase. Increasing the CTAB concentration in a slightly off-critical composition leads to the formation of vertical channels running from the top to the bottom of the membranes . Increasing the nanoparticle concentration leads to decreased coarsening of the membrane structure, which cause the membranes to have a lower pore size gradient over their thickness.

The STrIPS process was investigated by polymerization of membranes at different times after deposition. Analysis of these membranes using confocal and scanning electron microscopy showed that the water/BDA interface is initially stabilized very quickly and that phase separation progresses quickly through the membrane. This slows down deeper into the membrane, which is indicated by both the phase separation progressing slower, and the structure being more coarse. This is closely linked to the solvent diffusion out of the membrane, and it was attempted to correlate the progression of phase separation with a solvent diffusion model. The model did however predict faster solvent diffusion than experimentally observed, so further work is required to find out what causes the slower diffusion in the membrane.

The wetting of precursor dispersions on the PET substrate was investigated, as dewetting effects cause inhomogeneities in the membranes. It was found that more hydrophilic precursor compositions wet the substrate well, and that they result in membranes with nicely defined and straight edges, while the opposite is true for more hydrophobic precursor mixtures that wet worse and result in membranes with ragged edges. Furthermore, the wetting of a precursor mixture can be improved via the addition of CTAB to the continuous phase. Which can prove useful when the use of a badly wetting precursor is required for the structure it results in.

Aside from the progress made in better understanding bijel templated membranes, there are still areas where our understanding should be improved. The membrane structures should be tested for performance parameters in filtration, such as permeability, selectivity and mechanical strength. Furthermore, exchanging the substrate for porous PET could

maintain the unique properties of the membranes while improving their mechanical strength and preventing the damage that is currently caused by removing the membranes from the substrate.

Acknowledgements

First of all, I would like to than Martin for setting up this project, his helpful advice, and his boundless enthusiasm that always was a source of extra motivation. The next people I would like to thank next are my daily supervisors, Mariska and Henrik. They were always very helpful with answering my questions, explaining the difficult principles of our work, and showing me how to grow as a researcher. Georgios has done a lot of great work on his project that I continued working on, and helped me get a head start by explaining his work and with advice of how to continue the project. My sincere thanks to Alex, Dominique, and Bonny who keep our lab running and explained the many analysis techniques that we use at the lab. I am also grateful to everyone in the Haase group, for their input in our group meetings and for helping whenever I asked.

Everyone at FCC made me feel welcome in the year that I spent at the group, and ensured that we always had fun during the coffee breaks and delicious cakes on Fridays. Then a very special thanks to my fellow FCC master students, with whom I have had fruitful discussions about our work, but who most of all made me laugh and enjoy this year of research more.

Finally, I would like to thank all my friends and family for their support, and most of all my dad, who is not here to see me finally see me graduate, but who always believed I would when he was still alive.

Laymans summary

Het drinkbaar maken van zout en brak water wordt een steeds belangrijker proces door het toenemen van droogte en wereldbevolking. Dit kan gedaan worden door zout water te laten verdampen en het gecondenseerde stoom op te vangen, maar dit kost veel energie. Een manier die minder energie kost is om het water te filtreren door een membraan wat het zout tegen houdt. In deze thesis wordt een nieuw materiaal onderzocht dat gebruikt kan worden voor dit soort membranen. Het doel is om een productieproces te ontwikkelen waarmee we in staat zijn tot continue productie deze membranen, en om te begrijpen hoe we de interne structuur er van kunnen beïnvloeden. Dit is gedaan door met een van Lego gemaakte machine, verschillende membranen te produceren, en met behulp van verschillende microscopie technieken de structuur van de membranen te bepalen. Dit heeft geleid tot een beter begrip van het productieproces en de weg vrij gemaakt om deze membrane door te ontwikkelen.

Appendix A

Full overview of membranes made for the CTAB concentration variation study. Membranes are made with precursor dispersion compositions A and B, with particle weight fractions of 110 mg/g and CTAB concentrations ranging from 15 to 75 mM.
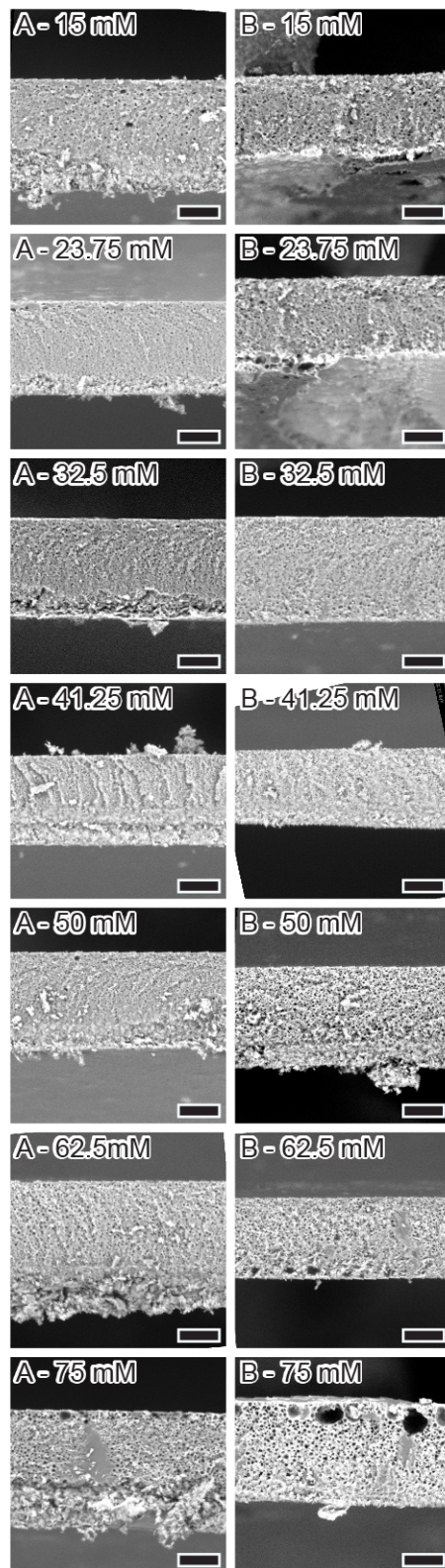
Figure 7.1: Scale bar is 20 µm.

Appendix B

Overview of the membranes polymerized at all the time steps from 600 ms to 10 s for membranes made with precursor dispersion composition D, with a particle weight fraction of 110 mg/g. CTAB concentrations are 50 and 15 mM for Figure 9.1 and 8.2 respectively.
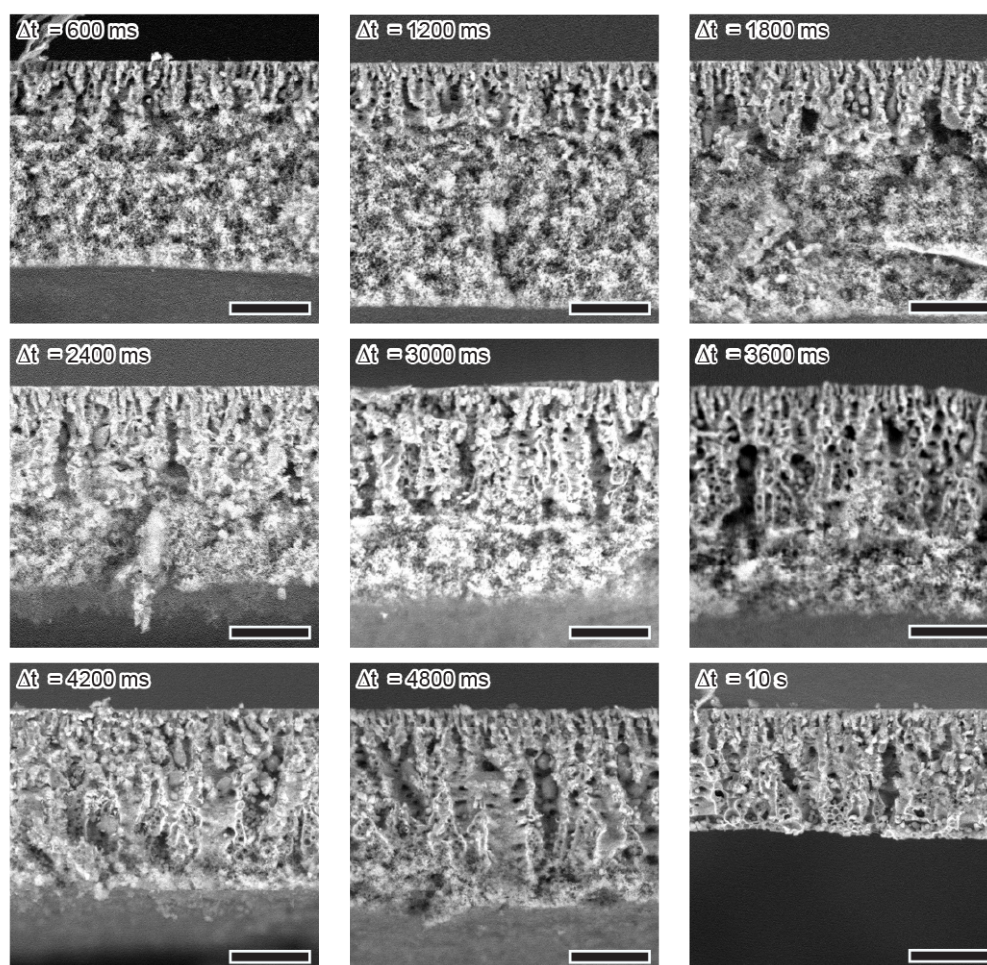

Figure 8.1: Membranes D - 50 mM CTAB - 110 mg/g nanoparticles polymerized at different indicated Δt. Scale bar is 20 µm.
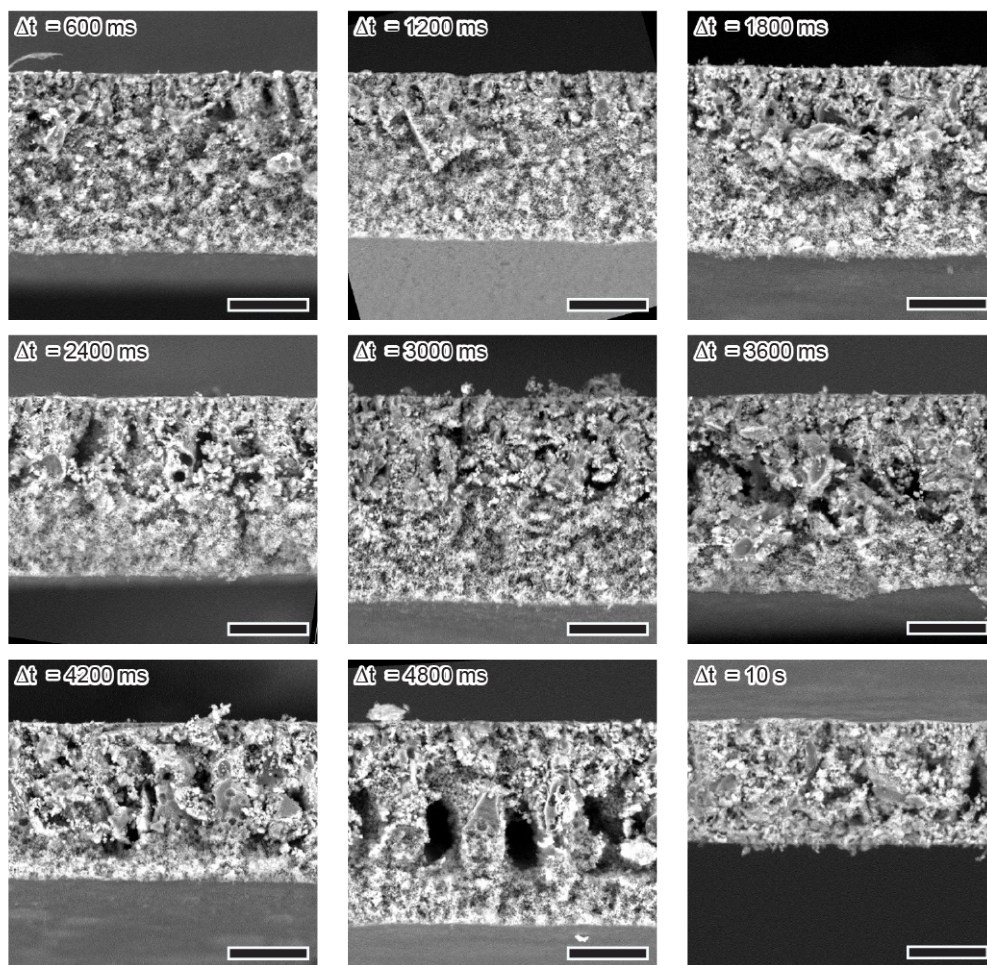
Figure 8.2: Membranes D - 15 mM CTAB - 110 mg/g nanoparticles polymerized at different indicated Δt.Scale bar is 20 µm.

Appendix C

Confocal images and 3D reconstructions of membranes made with composition C and D
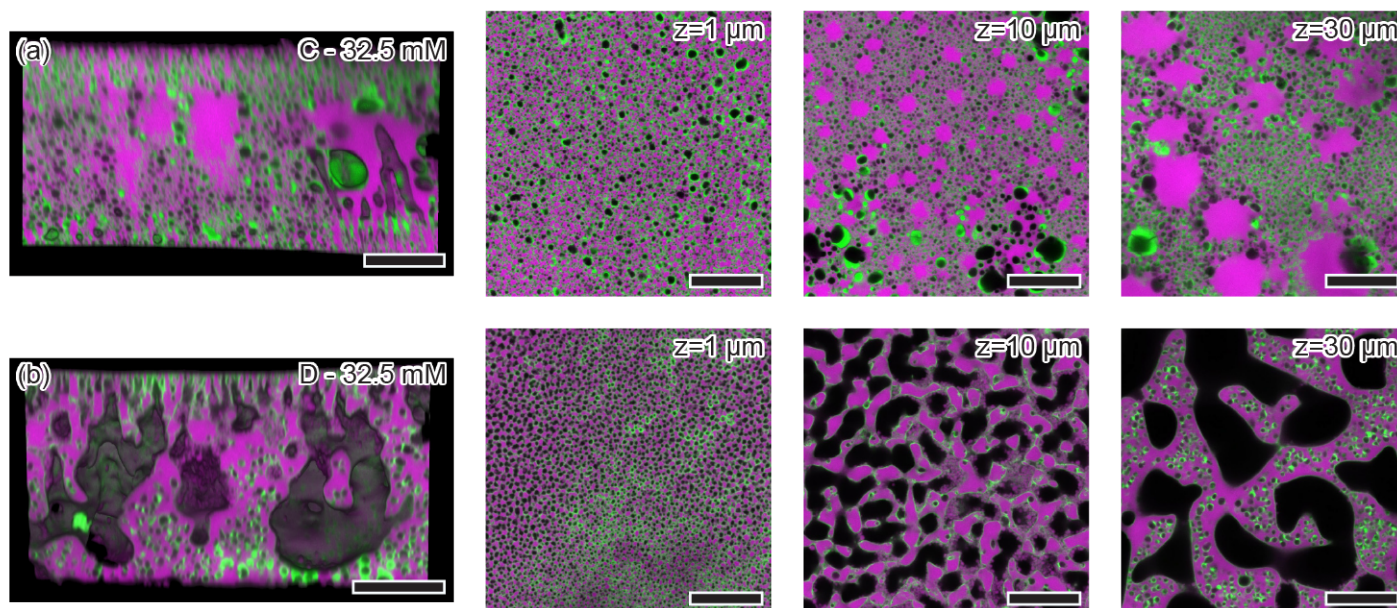with 50 mM CTAB and 110 mg/g nanoparticles.

Figure 9.1: Confocal images and 3D reconstructions of membranes made with composition
C (a), and D (b) with 50 mM CTAB and 110 mg/g nanoparticles. Confocal images are
taken at 1, 10, and 30 µm from the top surface of the membranes. Scale bar is 20 µm.

Bibliography

[1] Mark A. Shannon, Paul W. Bohn, Menachem Elimelech, John G. Georgiadis, Benito J. Mariñas, and Anne M. Mayes. Science and technology for water purification in the coming decades. *Nature*, 452(7185):301–310, mar 2008.

[2] Xiaolei Qu, Pedro J.J. Alvarez, and Qilin Li. Applications of nanotechnology in water and wastewater treatment. *Water Research*, 47(12):3931–3946, aug 2013.

[3] Muhammad Qasim, Mohamed Badrelzaman, Noora N. Darwish, Naif A. Darwish, and Nidal Hilal. Reverse osmosis desalination: A state-of-the-art review. *Desalination*, 459:59–104, jun 2019.

[4] Menachem Elimelech and William A. Phillip. The future of seawater desalination: Energy, technology, and the environment. *Science*, 333(6043):712–717, aug 2011.

[5] Heru Susanto and Mathias Ulbricht. Characteristics, performance and stability of polyethersulfone ultrafiltration membranes prepared by phase separation method using different macromolecular additives. *Journal of Membrane Science*, 327(1-2):125–135, feb 2009.

[6] Virender K. Sharma, Ria A. Yngard, and Yekaterina Lin. Silver nanoparticles: Green synthesis and their antimicrobial activities. *Advances in Colloid and Interface Science*, 145(1-2):83–96, jan 2009.

[7] Muzammil Anjum, R. Miandad, Muhammad Waqas, F. Gehany, and M.A. Barakat. Remediation of wastewater using various nano-materials. *Arabian Journal of Chemistry*, 12(8):4897–4919, dec 2019.

[8] Martin F. Haase, Kathleen J. Stebe, and Daeyeon Lee. Continuous fabrication of hierarchical and asymmetric bijel microparticles, fibers, and membranes by solvent transfer-induced phase separation (STRIPS). *Advanced Materials*, 27(44):7065–7071, oct 2015.

[9] Martin F. Haase, Harim Jeon, Noah Hough, Jong Hak Kim, Kathleen J. Stebe, and Daeyeon Lee. Multifunctional nanocomposite hollow fiber membranes by solvent transfer induced phase separation. *Nature Communications*, 8(1), nov 2017.

[10] Mohd A. Khan, Alessio J. Sprockel, Katherine A. Macmillan, Meyer T. Alting, Shankar P. Kharal, Stephen Boakye-Ansah, and Martin F. Haase. Nanostructured, fluid-bicontinuous gels for continuous-flow liquid–liquid extraction. *Advanced Materials*, 34(18):2109547, mar 2022.

[11] Henrik Siegel, Alessio J. Sprockel, Matthew S. Schwenger, Jesse M. Steenhoff, Iske Achterhuis, Wiebe M. de Vos, and Martin F. Haase. Synthesis and polyelectrolyte functionalization of hollow fiber membranes formed by solvent transfer induced phase separation. *ACS Applied Materials &amp Interfaces*, 14(38):43195–43206, sep 2022.

[12] Tiancheng Wang, Giuseppe Di Vitantonio, Kathleen J. Stebe, and Daeyeon Lee. Scalable manufacturing of hierarchical biphasic bicontinuous structures via vaporization-induced phase separation (VIPS). *ACS Materials Letters*, 2(5):524–530, apr 2020.

[13] G. Athanasiou. Fabrication of porous nanocomposite films via a continuous roll-to-roll process. Master's thesis, Utrecht University, 2022.

[14] K. Stratford, R. Adhikari, I. Pagonabarraga, J.-C. Desplat, and M. E. Cates. Colloidal jamming at interfaces: A route to fluid-bicontinuous gels. *Science*, 309(5744):2198–2201, sep 2005.

[15] E. M. Herzig, K. A. White, A. B. Schofield, W. C. K. Poon, and P. S. Clegg. Bicontinuous emulsions stabilized solely by colloidal particles. *Nature Materials*, 6(12):966–971, nov 2007.

[16] Kyle M. McDevitt, Daniel R. Mumm, and Ali Mohraz. Improving cyclability of ZnO electrodes through microstructural design. *ACS Applied Energy Materials*, 2(11):8107–8117, oct 2019.

[17] Sierra J. Gross, Kyle M. McDevitt, Daniel R. Mumm, and Ali Mohraz. Mitigating bubble traffic in gas-evolving electrodes via spinodally derived architectures. *ACS Applied Materials &amp Interfaces*, 13(7):8528–8537, feb 2021.

[18] Eric Dickinson. Food emulsions and foams: Stabilization by particles. *Current Opinion in Colloid &amp Interface Science*, 15(1-2):40–49, apr 2010.

[19] Hassan Firoozmand and Dérick Rousseau. Food-grade bijels based on gelatin-maltodextrin-microbial cell composites. *Food Hydrocolloids*, 48:208–212, jun 2015.

[20] Tharwat F. Tadros. *Topics in Colloid and Interface Science*. Wiley-VCH Verlag GmbH, 2012.

[21] Spencer Umfreville Pickering. CXCVI.—emulsions. *J. Chem. Soc., Trans.*, 91(0):2001–2021, 1907.

[22] Robert Aveyard, Bernard P Binks, and John H Clint. Emulsions stabilised solely by colloidal particles. *Advances in Colloid and Interface Science*, 100-102:503–546, feb 2003.

[23] Bernard P. Binks and Tommy S. Horozov. *Colloidal Particles at Liquid Interfaces*. Cambridge University Press, 2006.

[24] K Binder. Theory of first-order phase transitions. *Reports on Progress in Physics*, 50(7):783–859, jul 1987.

[25] Joe W. Tavacoli, Job H. J. Thijssen, Andrew B. Schofield, and Paul S. Clegg. Novel, robust, and versatile bijels of nitromethane, ethanediol, and colloidal silica: Capsules, sub-ten-micrometer domains, and mechanical properties. *Advanced Functional Materials*, 21(11):2020–2027, may 2011.

[26] Hua Hu and Ronald G. Larson. Marangoni effect reverses coffee-ring depositions. *The Journal of Physical Chemistry B*, 110(14):7090–7094, mar 2006.

[27] Ryan C. Rollings, Aaron T. Kuan, and Jene A. Golovchenko. Ion selectivity of graphene nanopores. *Nature Communications*, 7(1), apr 2016.

[28] Ho Bum Park, Jovan Kamcev, Lloyd M. Robeson, Menachem Elimelech, and Benny D. Freeman. Maximizing the right stuff: The trade-off between membrane permeability and selectivity. *Science*, 356(6343), jun 2017.

[29] Roar Søndergaard, Markus Hösel, Dechan Angmo, Thue T. Larsen-Olsen, and Frederik C. Krebs. Roll-to-roll fabrication of polymer solar cells. *Materials Today*, 15(1-2):36–49, jan 2012.

[30] Robert Abbel, Yulia Galagan, and Pim Groen. Roll-to-roll fabrication of solution processed electronics. *Advanced Engineering Materials*, 20(8):1701190, apr 2018.

[31] Robert Abbel, Ike de Vries, Arjan Langen, Gerwin Kirchner, Hero t'Mannetje, Harrie Gorter, Joanne Wilson, and Pim Groen. Toward high volume solution based roll-to-roll processing of OLEDs. *Journal of Materials Research*, 32(12):2219–2229, jun 2017.

[32] Roar R. Søndergaard, Markus Hösel, and Frederik C. Krebs. Roll-to-roll fabrication of large area functional organic materials. *Journal of Polymer Science Part B: Polymer Physics*, 51(1):16–34, oct 2012.

[33] Claudio F. Narambuena, Dante M. Beltramo, and Ezequiel P. M. Leiva. Polyelectrolyte adsorption on a charged surface. free energy calculation from monte carlo simulations using jarzynski equality. *Macromolecules*, 41(21):8267–8274, oct 2008.

[34] Yun Zhang, Hong Huang, Zhiling Liang, Houhe Liu, Ling Yi, Jinhong Zhang, Zhiqiang Zhang, Cheng Zhong, Yugang Huang, and Guodong Ye. Microscopic progression in the free radical addition reaction: modeling, geometry, energy, and kinetics. *Journal of Molecular Modeling*, 23(3), feb 2017.

[35] Christian Decker. The use of UV irradiation in polymerization. *Polymer International*, 45(2):133–141, feb 1998.

[36] Li Zhang, Qi Wang, Ying-Chun Liu, and Lian-Zhong Zhang. On the mutual diffusion properties of ethanol-water mixtures. *The Journal of Chemical Physics*, 125(10):104502, sep 2006.

[37] Wenjing Lu, Zhizhang Yuan, Yuyue Zhao, Hongzhang Zhang, Huamin Zhang, and Xianfeng Li. Porous membranes in secondary battery technologies. *Chemical Society Reviews*, 46(8):2199–2236, 2017.

[38] Muhammad Irshad Baig, Mehdi Pejman, Joshua D. Willott, Alberto Tiraferri, and Wiebe M. de Vos. Polyelectrolyte complex hollow fiber membranes prepared via aqueous phase separation. *ACS Applied Polymer Materials*, 4(2):1010–1020, jan 2022.

[39] Kroger, Martin, Editor Applied Rheology, and editors@appliedrheology.org. Shear rheology of silica nanoparticle dispersions. 2011.

[40] Shiv Govind Prasad, Abhijit De, and Udayan De. Structural and optical investigations of radiation damage in transparent PET polymer films. *International Journal of Spectroscopy*, 2011:1–7, apr 2011.

[41] Shankar P. Kharal and Martin F. Haase. Centrifugal assembly of helical bijel fibers for pH responsive composite hydrogels. *Small*, 18(11):2106826, jan 2022.